Journal of Controlled Release 379 (2025) 344–362

Contents lists available at ScienceDirect

Journal of Controlled Release

journal homepage: www.elsevier.com/locate/jconrel

Unveiling the drug delivery mechanism of graphene oxide dots at the atomic scale

Giulia Frigerio [a], Stefano Motta [b], Paulo Siani [a,c], Edoardo Donadoni [a], Cristiana Di Valentin [a,c,*]

[a] Department of Materials Science, University of Milano-Bicocca, Via R. Cozzi 55, I-20125, Milano, Italy
[b] Department of Earth and Environmental Sciences, University of Milano-Bicocca, Piazza della Scienza 1, I-20126, Milano, Italy
[c] BioNanoMedicine Center NANOMIB, University of Milano-Bicocca, Italy

ARTICLE INFO

Keywords:
Doxorubicin
Metadynamics
Nanomedicine
Controlled release
Active targeting

ABSTRACT

Graphene oxide (GO) is an amphiphilic and versatile graphene-based nanomaterial that is extremely promising for targeted drug delivery, which aims to administer drugs in a spatially and temporally controlled manner. A typical GO nanocarrier features a polyethylene glycol coating and conjugation to an active targeting ligand. However, it is challenging to accurately model GO dots, because of their intrinsically complex and not unique structure. Here, realistic atomistic GO models are designed as homogeneously/inhomogeneously oxidized flakes and then coated with stealth polymeric chains conjugated to an active targeting ligand (PEG-cRGD). Doxorubicin (DOX) adsorption is investigated by metadynamics simulations for accelerated loading/release events. The presence of PEG and cRGD are found not to affect the DOX adsorption, whereas the homogeneity of oxidation plays a crucial role. We also proved that a change in pH towards acidic conditions causes a reduction in the GO/DOX affinity in line with a pH-triggered release mechanism. Based on this study, the ideal graphene-based DOX carrier is identified as a homogeneously highly oxidized GO where graphitic regions with strong DOX π-π stacking are limited. Such interactions excessively stabilize DOX and are not weakened by a pH-change. On the contrary, DOX interactions with surface oxidized groups are H-bonding and electrostatic, which can effectively be modified by a pH reduction. Our findings are useful to the experimental community to further develop successful drug delivery systems.

1. Introduction

Targeted drug delivery is an administration approach that aims at enhancing the therapeutic efficacy, reducing the systemic side effects, and improving the patient compliance by precisely delivering medications to their intended sites of action within the body. [1] This strategy relies on nanomedical tools and can have a significant impact on the cancer treatment. Two-dimensional (2D) nanomaterials stand out as promising drug delivery platforms because of their large surface-to-volume ratio, [1,2] which allows for higher drug loadings compared to three-dimensional nanoparticles. [3,4] Among 2D nanomaterials, graphene oxide (GO) presents excellent properties for targeted drug delivery: high aqueous dispersibility, biocompatibility and tunable surface chemistry. [5,6]

GO is obtained from the oxidation of graphene, with the widely used modified Hummer's method [7] based on strong oxidants, such as MnO_4^-. [8,9] As a result, GO is a single layer of sp^2- and sp^3-hybridized carbon atoms, with a variety of oxygen-containing functional groups [10] and a size ranging from 1 nm^2 to 1 μm^2. [6] Even though the exact chemical structure of GO, in terms of the identity and arrangement of functional groups, is hard to uncover through experiments, its chemical composition is usually accessible by elemental analysis. The co-presence of unoxidized graphitic areas, as small as few square nanometers, with disordered oxidized regions has been observed through TEM experiments [10] and also predicted by ab initio calculations, [11] which found a strong correlation between oxidized sites, i.e. the oxidation barriers for carbon atoms neighboring already oxidized regions are lower. Consequently, GO not only inherits graphene optical/electronic properties and high mechanical strength, which make it appealing for many biomedical applications, such as bioimaging, [5] biosensing, [12] tissue engineering, [13] photodynamic [13] and photothermal therapy, [13] but, in addition to this, it bears plenty of functional groups, which are easy to functionalize and provide it with high hydrophilicity and colloidal stability. [5,14,15] Furthermore, it has been found that GO has

* Corresponding author at: Department of Materials Science, University of Milano-Bicocca, Via R. Cozzi 55, I-20125, Milano, Italy.
E-mail address: cristiana.divalentin@unimib.it (C. Di Valentin).

https://doi.org/10.1016/j.jconrel.2025.01.020
Received 2 September 2024; Received in revised form 16 December 2024; Accepted 8 January 2025
Available online 14 January 2025

a low affinity for the extremely abundant serum albumin protein, one of the proteins commonly found in the protein corona of nanomaterials, [16] and can cross the blood-brain barrier, delivering medications directly to the brain. [17–19] All these characteristics above make GO an ideal candidate for designing antitumor drug delivery systems, being a versatile nanomaterial that can be easily modified with stealth polymers to further improve its biocompatibility, as well as with active targeting ligands to achieve a higher drug concentration at the desired site of action. [20]

Indeed, several experiments have proven GO capable of loading chemotherapeutic drugs, which are often hydrophobic molecules, and delivering them in a controlled manner. [5,21,22] The most commonly loaded drug molecule is doxorubicin (DOX), an anthracycline antibiotic that works as a chemotherapeutic drug against several types of tumors, since, once internalized in the cancer cell nucleus, it intercalates between the DNA double-helix and inhibits its replication and thus the cell division process (cytostatic drug). [23,24] The loading of DOX on GO has resulted in improved anticancer efficacy for different reasons: an increased bioavailability compared to the liposomal-DOX counterpart was found for GO-DOX administered to breast cancer cellular models; [24] the ability to avoid drug multiresistance was proved for a GO-based DOX carrier functionalized with polyglycerol and a targeting peptide; [25] the co-delivery of the anticancer drug and a photosensitizer (Ce6) by a multimodal GO nanocarrier allowed for synergistic chemo- and photodynamic therapies. [26] It has been observed that DOX loading on and release from GO depend on the pH conditions. [23,27–29] The loading is favored around neutral pH, [27] whereas the release is favored at acidic pH, [23,27–29] like the one registered in the tumor microenvironment. This makes GO a stimuli-responsive drug carrier. A thermodynamic and kinetic study by Wu et al. [29] demonstrated that DOX spontaneously adsorbs on GO and proposed a Langmuir model, which implies that a DOX monolayer is adsorbed on GO. They suggested that the main GO/DOX interactions are electrostatic, between negatively charged GO and positively charged DOX molecules, together with intersystem hydrogen bonds. [29] Nevertheless, DOX adsorption on GO is believed to occur also by π-π stacking interactions. [30] Density Functional Theory (DFT) calculations showed that the adsorption of DOX on GO model surfaces is stronger on the sp^2 region (π-π stacking) than on the sp^3 one (hydrogen bonding). [31] Also, Mahdavi and coworkers [32] performed classical molecular dynamics (MD) simulations of DOX molecules on GO flakes with homogeneously arranged oxygen-containing groups at varying drug concentrations and pH values.

As mentioned above, the biocompatibility of GO is usually enhanced by coating with hydrophilic polymers, like polyethylene glycol (PEG) [9,20,22,23,26,33,34] or hyaluronic acid, [35] among others. The polymer coating is used to avoid dose-dependent cytotoxicity caused by GO-induced reactive oxygen species (ROS) production and oxidative stress. [5,6] Indeed, PEGylated GO was found to be substantially less prone to endocytic uptake by macrophages than uncoated GO. [36] DOX loading on PEGylated GO was also investigated at a computational level with classical MD simulations, suggesting a detrimental effect of the coating, which increases with the polymer chain length. [37,38]

Furthermore, to maximize the selectivity of the drug bioavailability at the desired site of action, GO nanocarriers are functionalized with active targeting ligands, whose high affinity for specific receptors overexpressed by target cells drives the accumulation of nanovehicles around them. The conjugation with different targeting ligands was reported for GO-based delivery systems: transferrin, a glycoprotein that binds to receptors overexpressed on glioma cells, was conjugated to PEGylated GO; [19] folic acid was conjugated to PEGylated GO to target folate-receptor-positive malignant cells and deliver two drug types simultaneously; [5,20] oligopeptides based on the RGD (Arg-Gly-Asp) sequence were used to target $\alpha_V\beta_3$ integrins, overexpressed by several types of solid tumors, [8,9,20,30,35,39–41] for which efficient drug delivery systems are needed because of the stiffness and limited permeability of their tissues.

However, a systematic computational exploration of DOX adsorption modes on realistic GO nanocarriers and an estimation of DOX adsorption free energy on GO are still missing. Notably, what distinguishes the computational models in this work, making them accurate GO nanocarriers models, are the following characteristics: (i) the oxidized areas co-exists with graphitic areas, as experimentally observed and as it has been done in only a few computational models so far, [42,43] (ii) the GO dot is not only coated with PEG chains, but also conjugated with a cyclic RGD (cRGD) targeting ligand, which was not yet ever included in previous computational work. In this context, we first build two 5 nm-wide GO flake-shaped models, also named *GO dots* for their sub-10 nm size, which differ in the arrangement of the oxygen functional groups. In the so-called *island* model, oxidized regions coexist with graphitic areas, whereas the *random* model is randomly oxidized. Both models are covalently functionalized with PEG chains or with PEG chains conjugated with cRGD targeting ligands, as commonly done experimentally for active targeting. [20] GO solvent accessibility, PEG conformation and cRGD ligand availability are evaluated by unbiased MD simulations. DOX loading on GO is investigated at physiological pH (7.4) and human body temperature (310 K), which are the conditions for DOX retention on GO, by means of metadynamics (MetaD) simulations, which is an enhanced sampling method widely applied for the investigation of drug binding to its target protein. [44–48] In this work, instead, MetaD is used to explore the drug adsorption to its nanocarrier, according to a protocol recently evaluated by our group. [49] A comparison of the adsorption modes and the corresponding DOX adsorption free energy is performed between (i) inhomogeneously (*island*) and homogeneously (*random*) oxidized bare GO dots and (ii) bare and cRGD-conjugated PEGylated GO dots. Moreover, the influence of a decrease in pH towards acidic conditions on DOX adsorption on the cRGD-conjugated PEGylated *island* GO dot was also assessed by MetaD simulations.

This study provides an accurate atomistic description of the intrinsically complex and inhomogeneous structure of GO and of DOX adsorption modes on GO, along with the evaluation of the effect of PEG and cRGD ligands on their occupancy, which are fundamental to identify the underlying factors driving the drug loading/release processes and, therefore, to design more efficient drug delivery nanomaterials.

2. Results and discussion

The main challenge in GO modeling consists in the determination of the type, number and arrangement of functional groups, given that the size of the system is known. Indeed, even though a general non-stoichiometric minimal formula of GO systems was recently proposed, i.e. $C_{1.5\text{-}2.5}H_{0.8}O_1$, [10] there is no unique structure and no repeating unit. In this scenario, throughout this work, we focus on the dependence of GO nanocarriers properties and drug loading capacity on the spatial arrangement of functional groups. To this aim, we use two types of GO structures, which differ only in the arrangement of the oxygen-containing functional groups, while sharing the same overall chemical composition ($C_{2.5}H_{0.8}O_1$), type (hydroxyl and epoxide groups on the basal plane and carboxyl and phenol hydroxyl groups on the edges) and number of functional groups. (i) In the *island* GO models (Fig. 1A–D), the groups are inhomogeneously arranged into graphitic and oxidized islands, in agreement with the experimental [10] and computational [11] evidence of their co-presence. (ii) In the *random* models (Fig. 1E–H), the functional groups are homogenously placed on GO surface, as it has been done in the majority of GO computational models designed so far to investigate biomedical applications. [32,37,38]

Before delving into our findings, it is helpful to present the nomenclature used in this work (Fig. 1). GO_i indicates the bare (uncoated) *island* GO model (Fig. 1B), in which graphitic and oxidized areas ("islands") coexist – a similar model in terms of group arrangement was previously referred to as *semiordered*; [43] GO_r indicates the bare (uncoated) *random* GO model (Fig. 1F), whose surface is randomly and homogeneously oxidized. GO_i-PEG (Fig. 1C) and GO_r-PEG (Fig. 1G)

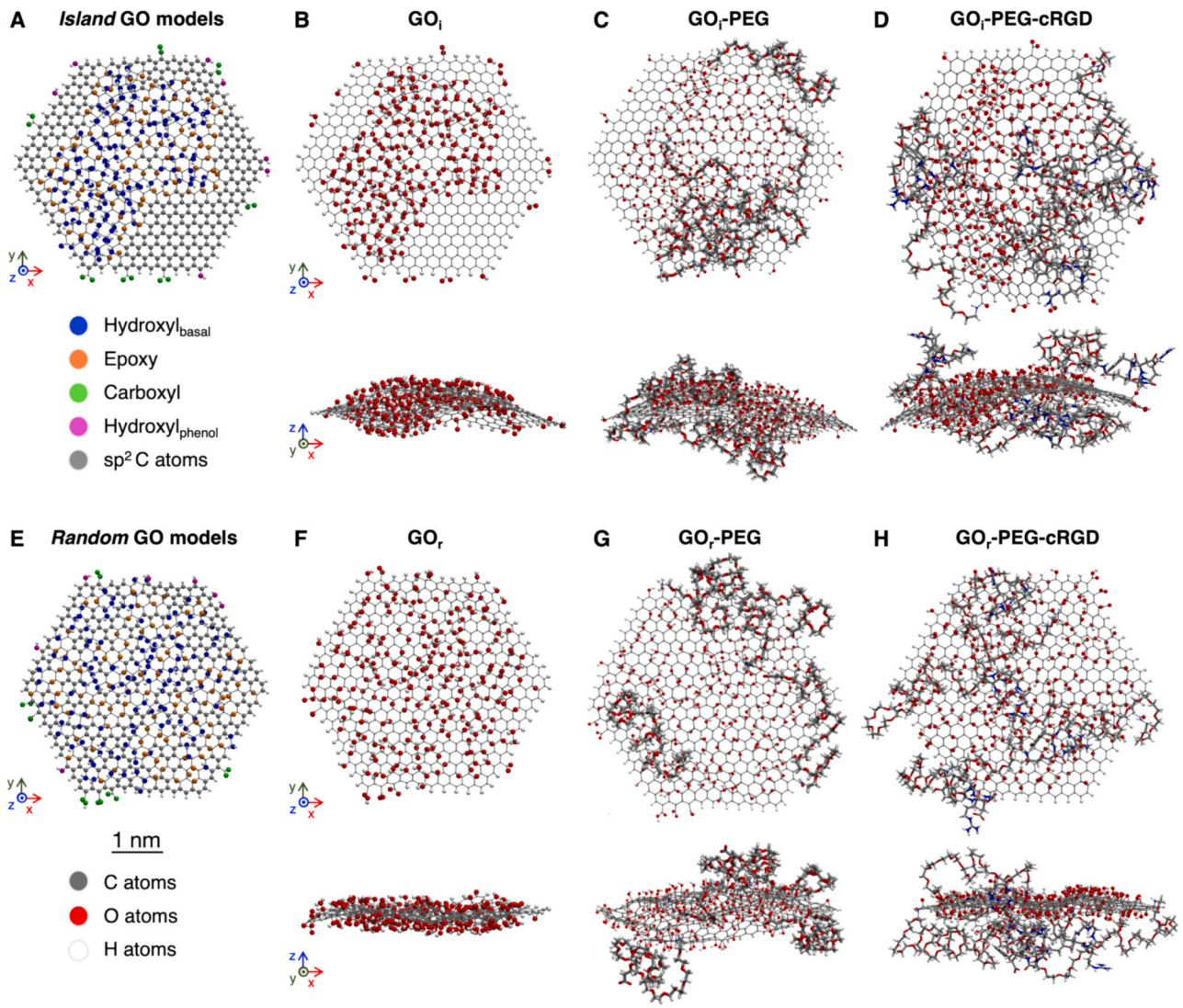

Fig. 1. Representation of the equilibrated structures of all GO models considered in this work, at the end of the production phase. (A-D) Top and side views of structures of *island* GO models: (A) bare GO_i structure with C and O atoms colored according to the type of functional group they belong to, (B) bare *island* GO (GO_i), (C) PEGylated *island* GO (GO_i-PEG) and (D) cRGD-conjugated PEGylated *island* GO (GO_i-PEG-cRGD). (*E*-H) Top and side views of structures of *random* GO models: (E) bare GO_r structure with C and O atoms colored according to the type of functional group they belong to, (F) bare *random* GO (GO_r), (G) PEGylated *random* GO (GO_r-PEG) and (H) cRGD-conjugated PEGylated *random* GO (GO_r-PEG-cRGD). Color codes are on the left. Water and ions are not shown for clarity. The two MD simulation replicas performed for each model give similar results and therefore we only show the structures of replica (i).

stand for the PEGylated *island* and *random* GO models with four PEG chains, respectively. GO_i-PEG-cRGD (Fig. 1D) and GO_r-PEG-cRGD (Fig. 1H) stand for cRGD-conjugated PEGylated *island* and *random* GO models, respectively. cRGD is the short form of c(RGDyK), which is the complete sequence of the cyclic pentapeptide considered in this work. The complexes of DOX with GO_i, GO_r and GO_i-PEG-cRGD are referred to as GO_i/DOX, GO_r/DOX and GO_i-PEG-cRGD/DOX, respectively.

The remainder of this section is organized as follows. In Section 2.1 the structural features and solvent interaction of GO_i and GO_r are compared. Section 2.2 includes the structural and conformational analysis of *island* and *random* GO dots functionalized with PEG chains and conjugated with cRGD targeting ligand, focusing on PEG conformation and cRGD availability. In Section 2.3 the drug loading process on bare and functionalized GO dots is studied from an atomistic and energetic point of view. To this purpose, DOX is loaded on GO_i, GO_r and GO_i-PEG-cRGD at neutral pH (7.4) and on GO_i-PEG-cRGD at slightly acidic pH (5.5).

2.1. *Effect of oxidation (in)homogeneity on the structure and solvation of bare GO dots*

At an initial level, we evaluate the effect of oxygen-containing functional groups arrangement on the structural properties and solvation of the two simplest GO dot models considered in this work: GO_i and GO_r in Fig. 1 (see Methods Section 4.1, Table 5 and Table S6 for further model details). According to the TEM microscopic images, [10] the *island* model is the most realistic and accurate, whereas the *random* model is regarded as a comparative reference model and reproduces the so-far most common approach of arranging functional groups in existing computational studies of GO. The size of the models (5 nm) is close to the smallest experimentally achievable one [50] and allows to include graphitic islands of a realistic size (1-2 nm wide). [10,23] Almost all COOH edge groups are deprotonated, according to their acidity at physiological pH (7.4), [51] yielding a charge density of —51 C g^{-1}, in perfect agreement with that determined by Konkena et al. [51] at neutral pH from titration experiments. We refer to Section 4.1 for a thorough description of how GO models were built and of their

characteristics.

Two replicas of a 100 ns-long MD simulation are run for each bare GO dot in an aqueous solution at physiological temperature and ionic strength conditions (see computational details in Section 4.2). A first general structural assessment based on the side views of the equilibrated structures in Fig. 1B and F indicates that both graphene oxide models wrinkle. This is expected since sp^3-hybridized carbon atoms tend to adopt a slightly distorted tetrahedral geometry causing the wrinkling of the flake. Despite being classified among 2D nanomaterials, GO dots have a non-zero dimension along the direction perpendicular to the plane, even at the small flake size considered in this work. The extent of GO wrinkling depends on the oxidation process and on the oxidized groups spatial arrangement. Indeed, the *island* model features a wide convex area surrounded by flat graphitic regions, which results in a slightly larger average thickness than the one of GO_r (Table 1). Nevertheless, both thickness values are within the experimentally range of 8-18 Å [27,33,52–56] and the structural deformation of the GO sheet calculated in Ref. [57], which is in the range of 8 Å. Due to the structural origin of GO wrinkling, the average deviation from the equilibrated structure along the simulation is quite low (Root Mean Squared Displacement (RMSD) of 0.5 (± 0.1) Å and 0.6 (± 0.1) Å for both replicas of GO_i and GO_r, respectively). The sub-angstrom RMSD values correspond to a low structure flexibility in water, which is in line with the low Root Mean Squared Fluctuation (RMSF) values shown in Fig. S1.

Secondly, it is worth comparing GO_i and GO_r with respect to the interaction with the surrounding solution, by evaluating the Solvent Accessible Surface Area (SASA), the H-bonds and the radial distribution function, g(r). The SASA is a commonly used descriptor of the solvation. [58] Despite the identical chemical composition, the GO_r presents a higher SASA value by nearly 300 $Å^2$ and a greater contribution of the oxidized areas to the overall SASA (Table 1). Moreover, we find a greater number of intramolecular H-bonds for GO_i than for GO_r which is more involved in H-bonds with water (Fig. S2). This trend in the GO/solvent H-bond number can be rationalized by the fact that in the *island* model the same number of groups is confined to a smaller area and then the groups are closer to each other and less accessible to the solvent, in agreement with ab initio MD simulations. [43]

The g(r) of water and ions around the GO dot is informative of GO solvation (Fig. S3). The location of g(r) peaks and their relative intensity is similar to the one registered in Refs. [57, 59] As expected, the intensity of the first g(r) peak follows the order carboxyl > phenol hydroxyl > basal hydroxyl > epoxide, with the graphitic sp^2 C atoms being the less hydrated species. In line with the higher solvent accessibility of the O groups on the *random* model, the first peak intensity of water surrounding both hydroxyl and epoxide groups in GO_r is higher than in GO_i (Fig. S3). Furthermore, the less dense group arrangement of the *random* model makes it more available to Na^+ ions, which are attracted by the negative charge of GO (Fig. S3). In fact, the integral of Na^+ g(r) summed up to 3 Å from GO atoms is equal to 2 Na^+ and almost 4 Na^+ for GO_i and GO_r, respectively. On the contrary, the integral of Cl^- g(r) is essentially zero for both because of the coulombic repulsion.

Overall, we can conclude that different groups arrangements on GO have a non-negligible effect on their accessibility and interaction with the solution. In the *island* model, which should better reproduce a realistic GO structure, the oxygen atoms have lower solvent accessibility than in the *random* one. Therefore, in GO computational modeling it is critical to arrange the groups in agreement with experimental evidence. The differences in the surface solvation may cause different conformations of the polymer coating (Section 2.2) and, more importantly, different GO drug loading ability (Section 2.3).

2.2. PEG conformation and active targeting ligand availability on GO dots

As mentioned in the introduction, in biomedical applications, GO is typically coated with biocompatible polymers and, eventually, conjugated with active targeting ligands to improve its biocompatibility and selectivity for the diseased tissues. In this work, to model a proper GO nanocarrier, we functionalize GO dots with PEG and cRGD (structural formulas in Fig. S4C), as a representative polymer and targeting ligand, respectively. The aim of this section is therefore to examine PEG conformation on GO and cRGD availability, which are crucial but experimentally hard-to-be-determined descriptors.

We PEGylated both GO_i and GO_r without and with active targeting ligands: (i) the simpler systems, GO_i-PEG and GO_r-PEG (Fig. 1C,G), are composed by the *island/random* GO dot covalently functionalized with NH_2-PEG_{1000}-COOH chains, which bear a molecular weight of 1000 g mol^{-1}; (ii) the more comprehensive models, GO_i-PEG-cRGD and GO_r-PEG-cRGD (Fig. 1D,H), consist in the *island/random* GO dot covalently functionalized with NH_2-PEG_{1000}-cRGD chains. The degree of functionalization corresponds to 25 % wt of PEG over GO-PEG, which agrees with the experimentally achievable grafting density. [20,33,40,54,55] In particular, two chains are connected to the basal plane through a secondary amine functionality and the other two are bonded to the edge with amide functionalities. We refer to Section 4.1 for further details on the models design and to Section 4.2 for simulation details. Two replicas of 150 ns-long MD simulations are performed for each model and a representative structure for each model is represented in Fig. 2.

First, we focus on the behavior of PEGylated GO models in solution. Obviously, PEGylated GO dots are thicker than bare ones with thickness values (Table 1) that fall in the range of those experimentally registered by AFM measurements for similar structures (16-41 Å). [33,54,55] Even though GO SASA (Table 1) is reduced upon coating with PEG to nearly 70 % or 80 % of the value for bare GO_i and GO_r, respectively, the majority of GO surface is still accessible to the solvent and, potentially, to drugs for their loading. In other words, PEG chains only partially cover the GO surface, as evident in Fig. 2. The question is whether PEG

Table 1
Average thickness and SASA of bare (GO_i and GO_r), PEGylated (GO_i-PEG and GO_r-PEG) and cRGD-conjugated PEGylated (GO_i-PEG-cRGD and GO_r-PEG-cRGD) models.

Property	Thickness [Å]	SASA [$Å^2$]	SASA/$SASA_{bare}$ %	$SASA_{oxid}$:$SASA_{grap}$ (%)
GO_i (i)	(11.7 (± 0.5))	5700 (± 100)	100 %	63:37
GO_i (ii)	(11.7 (± 0.4))	5700 (± 100)	100 %	63:37
GO_r (i)	(9.0 (± 0.7))	5980 (± 70)	100 %	77:23
GO_r (ii)	(9.1 (± 0.7))	5980 (± 70)	100 %	77:23
GO_i-PEG (i)	(24 (± 4))	4100 (± 100)	72 %	67:33
GO_i-PEG (ii)	(25 (± 5))	4100 (± 100)	72 %	67:33
GO_r-PEG (i)	(28 (± 4))	4800 (± 100)	80 %	76:24
GO_r-PEG (ii)	(28 (± 4))	4800 (± 100)	80 %	75:25
GO_i-PEG-cRGD (i)	(30 (± 6))	3680 (± 90)	65 %	64:36
GO_i-PEG-cRGD (ii)	(29 (± 7))	3800 (± 100)	67 %	63:37
GO_r-PEG-cRGD (i)	(31 (± 4))	4400 (± 70)	74 %	72:28
GO_r-PEG-cRGD (ii)	(31 (± 4))	4300 (± 100)	72 %	73:27

Each value is obtained as the average and its standard deviation over the production phase (last 50 ns of MD simulation). SASA/$SASA_{bare}$ % is the percentage of GO SASA still available upon functionalization. $SASA_{oxid}$:$SASA_{grap}$ is the ratio between the contribution of oxidized areas and of graphitic areas to the SASA. Further details on the analyses are in Section 4.2. The values for both replicas (i, ii) are reported.

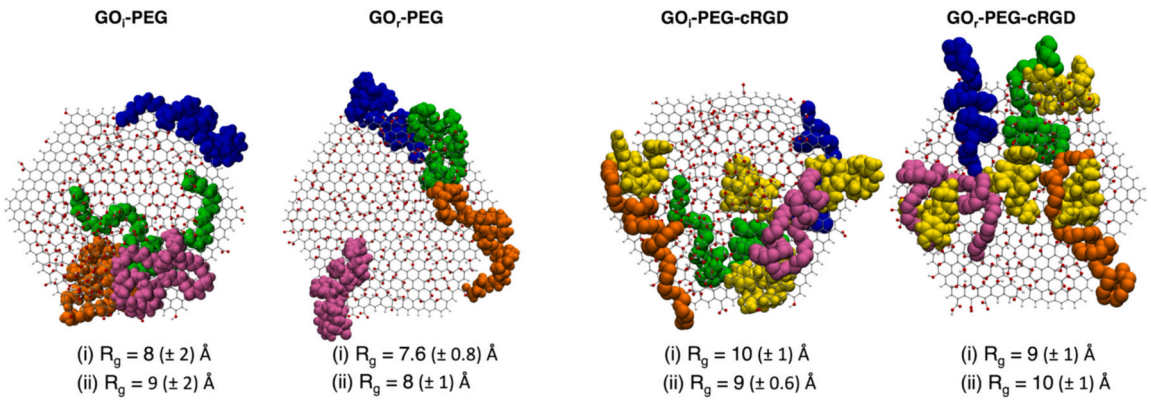

Fig. 2. Representation of the equilibrated structures of PEGylated and cRGD-conjugated PEGylated GO models where each PEG/PEG-cRGD chain is shown with van der Waals spheres of a different color and cRGD ligands are highlighted in yellow, along with the average R_g values and their standard deviation of PEG and PEG-cRGD chains for both replicas (i, ii). The latter ones are obtained as the average among the four polymeric chains over the production phase of each replica (see Fig. S5 for radius of gyration as a function of time). Color code: carbon atoms in grey, oxygen atoms in red and hydrogen atoms in white. Water and ions are not shown for clarity. The two replicas look similar and therefore we only represent one structure per replica. (For interpretation of the references to color in this figure legend, the reader is referred to the web version of this article.)

interacts with the graphitic and/or the oxidized domains to the same/different extent. This aspect is crucial for the assessment of the stealth effect of PEGylation and preliminary to the discussion on drug loading in Section 2.3. Interestingly, the ratio between the contribution of oxidized and graphitic areas to the SASA is almost the same for the bare and the PEGylated *random* models, whereas it goes from 63:37 to 67:33 upon PEGylation of the *island* model. This suggests that PEG interacts with the graphitic areas to a greater extent than with the oxidized regions. Moreover, different descriptors point to a greater interaction of PEG with GO$_i$ rather than with GO$_r$: the lower percentage of bare GO SASA still accessible to the solvent after PEGylation (72 % for GO$_i$ vs 80 % for GO$_r$), the slightly higher intensity of the PEG number density around GO$_i$ (Fig. 3A) and the stronger PEG/GO$_i$ non-bonded interaction energy (Table 2, Fig. S6), which is calculated as the sum of the van der Waals and the electrostatic contributions. On the other hand, the non-bonded interaction energy of PEG with the solution is stronger for GO$_r$-PEG than for GO$_i$-PEG. Lastly, a measure of the conformation of PEG around the GO dot can be obtained by the radius of gyration, whose value in Fig. 2 is in line with that registered for a single PEG$_{1000}$-COO$^-$ chain in solution (10 (± 2) Å) in a previous work by some of us, [60] meaning that the PEG conformation is not affected upon linking to GO.

The fact that PEG mainly interacts with the unoxidized regions of GO

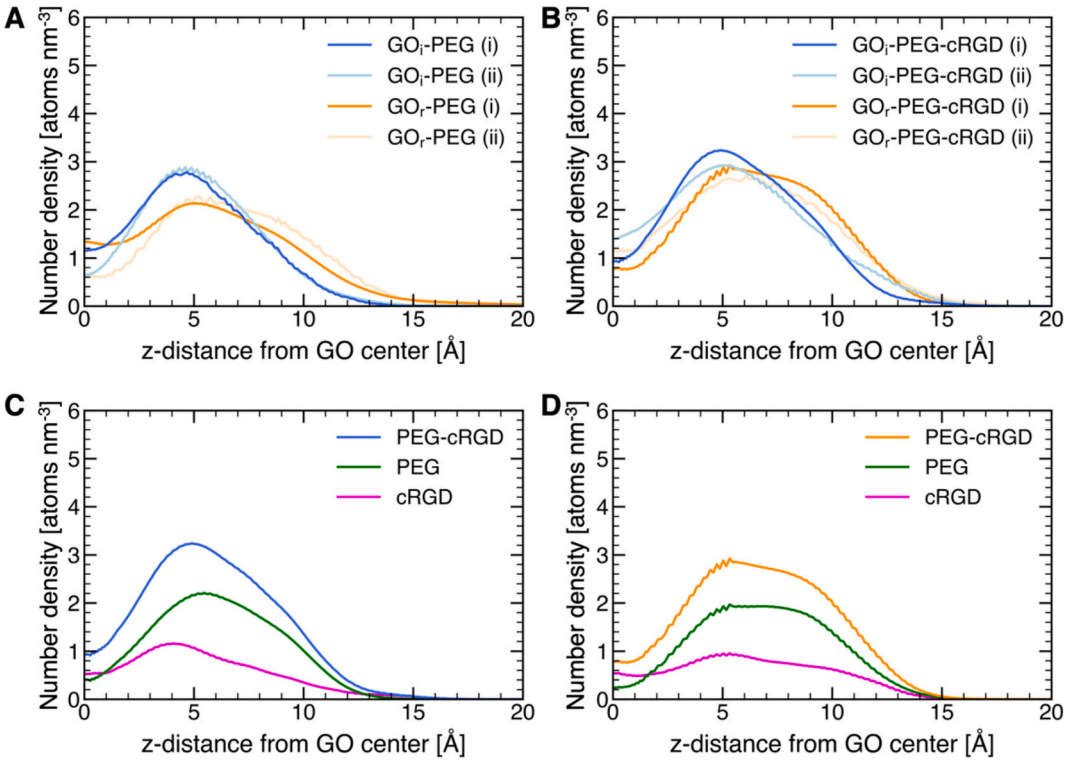

Fig. 3. Number density profiles of PEGylated and cRGD-conjugated PEGylated GO models along *z*-distance from GO center, i.e. perpendicularly to the GO flake. (A) Number density profiles of PEG for the production phase of the two replicas (i, ii) of each GO-PEG simulation. (B) Number density profiles of PEG-cRGD for the production phase of the two replicas (i, ii) of each GO-PEG-cRGD simulation. (C,D) Number density profiles for PEG-cRGD and its cRGD and PEG contributions for the first replica of GO$_i$-PEG-cRGD and GO$_r$-PEG-cRGD, respectively. The profiles for the second replica look similar and are not reported.

Table 2
Non-bonded interaction energy between PEG or cRGD molecules and GO dot or the aqueous solution.

Energy [kcal mol^{-1}]	GO-PEG		GO-PEG-cRGD			
	PEG/GO	PEG/solution	PEG/GO	PEG/solution	cRGD/GO	cRGD/solution
Island (i)	–28 (± 4)	–305 (± 9)	–24 (± 3)	–316 (± 10)	–34 (± 2)	–151 (± 8)
Island (ii)	–31 (± 4)	–327 (± 10)	–10 (± 3)	–327 (± 9)	–29 (± 3)	–134 (± 10)
Random (i)	–3 (± 4)	–348 (± 10)	–3 (± 3)	–316 (± 10)	–20 (± 2)	–173 (± 8)
Random (ii)	–6 (± 4)	–354 (± 10)	–6 (± 3)	–302 (± 9)	–19 (± 3)	–173 (± 10)

The values are the sum of the van der Waals and the electrostatic contributions. The average over the production phase (last 50 ns of 150 ns) with the standard deviation is reported. The values are normalized over the number of PEG or PEG-cRGD chains. The values for both replicas (i, ii) are reported. The plots of the non-bonded interaction energies as a function of the simulation time can be found in Fig. S6. A complementary H-bonds analysis can be found in Table S1.

may seem counterintuitive, as one would expect PEG to prefer oxidized areas or to be solvated and less prone to interact with hydrophobic species, given its polar character. Nevertheless, it should be considered that the competition for the interaction with graphitic areas of GO is among PEG and the solution, which is essentially water in this case. However, PEG is undoubtedly less polar than water and, therefore, it tends to screen the GO graphitic area. Indeed, the hydrophobic unoxidized regions can be easily recognized by serum proteins, which may lead to the formation of a hard protein corona [61] and the role of the polymer coating is exactly to prevent this from happening, providing the nanomaterials with stealth properties.

Secondly, we perform a structural, conformational and energetic analysis of cRGD-conjugated PEGylated GO systems, where each PEG chain is linked to a cRGD ligand at its terminal end in solution (Fig. 1D, H). As expected, the average thickness is greater than the one of PEGylated GO (Table 1). The GO SASA further reduces to ~66 and ~ 73 % of the bare GO SASA for *island* and *random* models, respectively. In this case and differently from the PEG case, the ratio between oxidized and unoxidized regions contributing to the SASA is similar to the one of bare GO dots, which means that cRGD ligands balance the above-discussed difference in the PEG interactions with oxidized and unoxidized areas. Also, according to the average non-bonded interaction energies in Table 2 and their time evolution in Fig. S6, it emerges that cRGD has a slightly higher affinity for the solvent than for the GO surface in the *random* models.

Among different fragments of the cRGD ligand, the two components whose interaction with GO is maintained for most of the production phase are the tyrosine side chain (through π-π stacking interactions with the unoxidized regions) and the cyclic backbone (through H-bonds with the oxygen-containing functional groups), see Table S2. Arg and Asp side chains interact with GO for a smaller fraction of the production phase (Table S2), which is promising, since these aminoacids are involved in the interaction with the target integrin and, therefore, a prolonged binding to GO surface would be detrimental to their targeting activity.

To assess cRGD availability, we decompose the number density profile of the PEG-cRGD chains (Fig. 3B) into its PEG and cRGD contributions (Fig. 3C,D). The maximum peak of the cRGD profile is located at a similar normal distance from GO as that of the PEG profile. cRGD clearly interacts with GO while is also considerably solvated, as indicated by the non-bonded interaction energies with the solution (Table 2, Fig. S6). Therefore, we can conclude that while the availability of cRGD for interaction with the target integrins may be somewhat limited by the potential adsorption to GO surface, it is not significantly hampered.

Taken together, we find that PEG interacts with GO surface to a greater extent in the *island* model than in the *random* one and adsorbs also on the unoxidized regions thanks to hydrophobic forces. cRGD targeting ligands, conjugated to PEG chains, interact both with the GO surface and with the aqueous solution. The GO surface is still accessible to the solvent for at least 65 % of the total SASA of the corresponding bare model, even upon functionalization with PEG-cRGD chains. A good solvent accessibility is a requirement for drug loading, which is investigated in the next section.

2.3. Doxorubicin loading on/release by GO nanocarriers

Here, DOX is taken as a model chemotherapeutic drug to probe GO drug adsorption sites. To this aim, among the six GO models in Fig. 1, we only consider the following as potential drug nanocarriers: the bare *island* and *random* GO dots (see Section 2.1 for further details on these models) and the cRGD-conjugated PEGylated *island* GO dot (see Section 2.2 for further details on this model). The latter is simulated both at physiological (7.4) and at slightly acidic (5.5) pH to assess the effect of a pH change on DOX adsorption.

To calculate the DOX adsorption free energy to different GO nanocarriers and achieve an atomistic understanding of DOX adsorption modes, we performed a set of MetaD simulations following a protocol evaluated by our group. [49] The use of an enhanced sampling method, such as MetaD, is further justified by the fact that in the preliminary unbiased MD simulations a DOX molecule in solution with a GO dot readily loads on the nanomaterial (see also Section 4.3). However, it does not diffuse on the surface fast enough to explore different adsorption sites within a reasonable computational time (see Fig. 4B, Fig. 4C and Fig. S7). Instead, in MetaD simulations, where a bias potential is applied to the collective variable (CV), *d*, i.e., the distance between the center of DOX ring *C* (the center of DOX aromatic portion in red in Fig. 4A) and the closest GO carbon atom (Fig. 4A), multiple adsorption events are registered (Fig. 4D–F). This is true for different regions of the GO dot, both above and below the plane, and for all the three systems considered (Fig. 4G–I). The high number of transitions between adsorbed and not-adsorbed states and the spatially homogeneous sampling of the GO surface are required to obtain a reliable estimate of the DOX adsorption free energy. We refer to Section 4.3 for further details about MetaD simulations setup and analysis.

In this following, we only discuss GO_i/DOX, GO_r/DOX and GO_i-PEG-cRGD/DOX systems at physiological pH, and we refer to Section 2.3.3 for the simulations at acidic pH. First, we can say that DOX loading on bare and functionalized GO is a spontaneous process at neutral pH, according to the wide minimum well in the free energy profiles in Fig. 5 and the negative adsorption free energy values in Table 3. Interestingly, we find that DOX has a different affinity for the three nanocarriers considered here, following the order: GO_i > GO_i-PEG-cRGD > GO_r. Experimentally, a standard adsorption free energy, ΔG_a^0, of –5.9 kcal mol^{-1} was calculated from the equilibrium constant K_a^0 ($\Delta G_a^0 = -RT \ln K_a^0$) at 310 K – the same temperature used in our MetaD simulations – by Wu et al. [29] for DOX on bare and highly oxidized GO (estimated C/O ratio = 1.2 from elemental analysis data).The experimental ΔG_a^0 lies between the calculated adsorption free energy for GO_i and GO_r. For any discrepancy from the calculated values, it must be mentioned that the GO sample used experimentally has a higher extent of oxidation than the one used in this work, according to the C/O ratio resulting from its elemental analysis (experimental C/O = 1.2 vs model C/O = 2.5). Also, it should be noted that experimentally more DOX molecules are loaded: one DOX molecule, which corresponds to a 0.05 mg/mg (DOX/GO) loading capacity for bare GO models, is well below the maximum adsorption capacities registered experimentally, which range from 1.43 mg/mg (DOX/GO), as estimated from the Langmuir isotherm model,

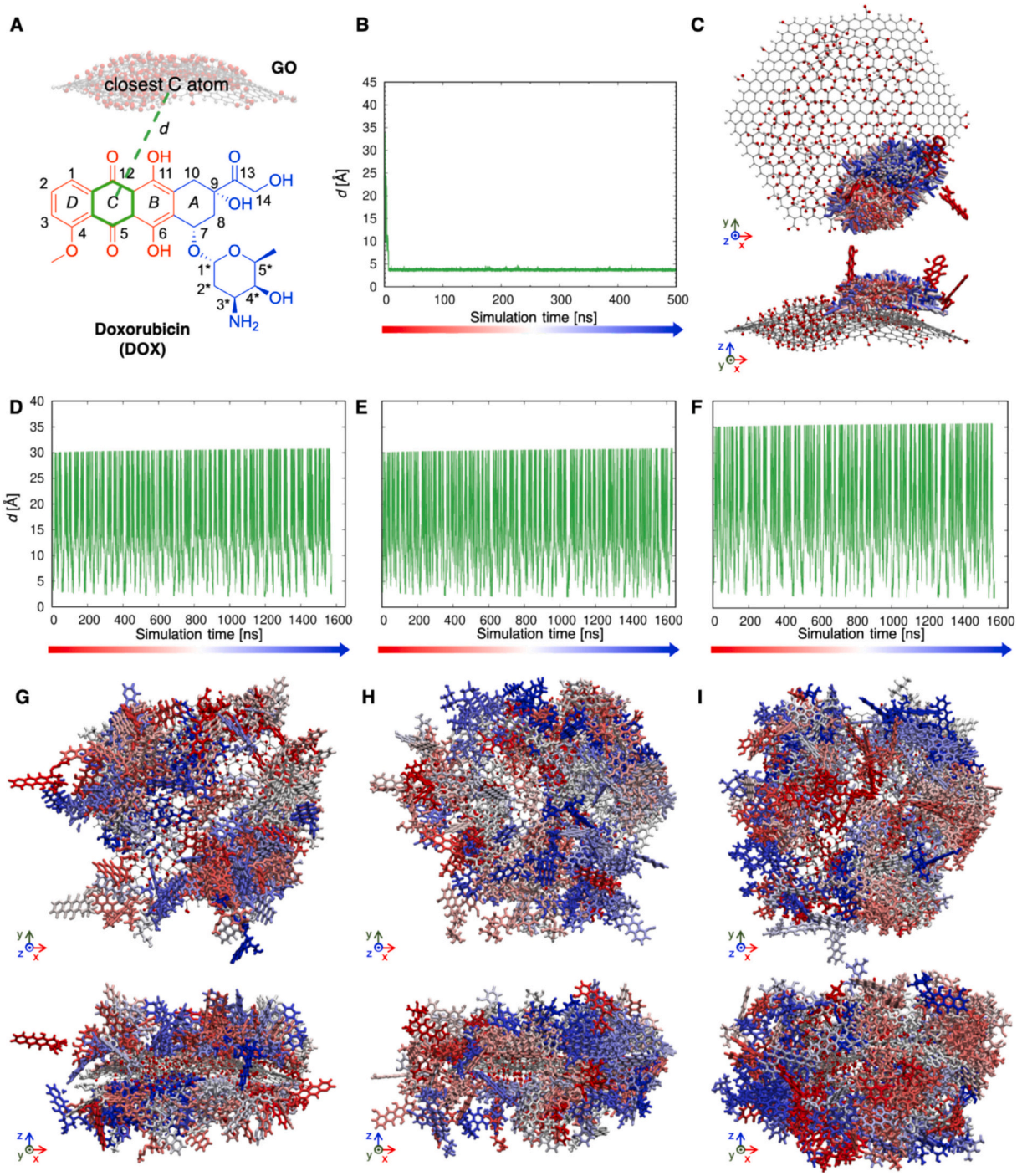

Fig. 4. (A) Representation of the collective variable *d* biased along the MetaD simulations performed at physiological pH (7.4) in this work. In the DOX structural formula, the aromatic fragment, i.e. three aromatic planar rings (hydroxyanthraquinone, is represented in red and the hydrophilic portion, i.e. a non-planar ring linked to an amino-glycosidic side chain (daunosamine), in blue. (B) Values of *d* and (C) top and side views of DOX adsorption to GO dot along one of the three unbiased MD simulation runs for GO_i/DOX complex. See Fig. S7 for the other two, starting from different starting point relative orientations. (D,E,F) Values of *d* and (G,H,I) top and side views of the regions where DOX binds along the MetaD simulations of GO_i/DOX, GO_r/DOX and GO_i-PEG-cRGD/DOX systems, respectively. DOX molecules are represented at different simulation times and colored according to the simulation evolution, i.e. from red to blue as the simulation time increases. In GO_i-PEG-cRGD/DOX representation, PEG-cRGD chains are omitted for clarity. Water and ions are not shown for clarity. (For interpretation of the references to color in this figure legend, the reader is referred to the web version of this article.)

[29] to 2.35 mg/mg (DOX/GO), for an initial DOX concentration of 0.47 mg/mL. [27] Therefore, DOX-DOX interactions may also play a role in determining the experimental ΔG_a^0.

Secondly, not only different nanocarriers present different DOX adsorption free energy, but there are also multiple minima for the same nanocarrier (Fig. 5). We should stress that, according to the definition of the CV *d*, the minimum location is defined by the distance of the center of mass of the aromatic portion of DOX from the carbon atoms backbone of GO. To unveil the atomistic details of different adsorption modes and find the recurrent features for DOX adsorption on GO dots, we train a self-organizing map (SOM) with a set of DOX-GO intermolecular distances, which are independent of the model considered (Fig. S9). We

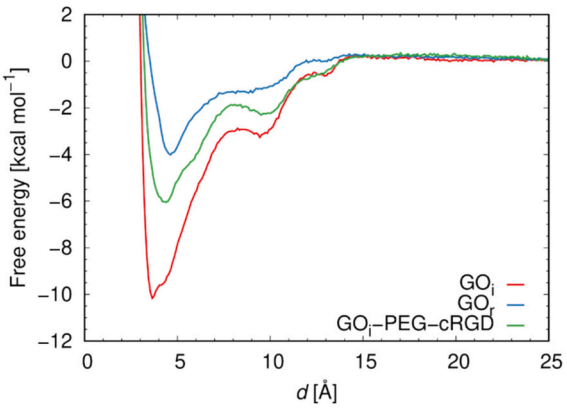

Fig. 5. Free energy profiles of DOX loading on GO_i, GO_r and GO_i-PEG-cRGD. Increasing values of the distance *d* correspond to the DOX aromatic portion moving away from the GO surface towards bulk solution. Each of the profiles is calculated as the average from 800 ns to the end of the simulation time.

Table 3
Adsorption free energy, ΔG_a, of DOX on GO models.

Model	ΔG_a [kcal mol^{-1}]
GO_i	–10.4 (± 0.1)
GO_r	–3.9 (± 0.1)
GO_i-PEG-cRGD	–6.8 (± 0.1)
GO_i(COOH)-PEG-cRGD	–6.6 (± 0.1)
GO_i(COOH/OH)-PEG-cRGD	–6.4 (± 0.1)

The value is the average from 800 ns and it is calculated from the integration of the profiles in Fig. 5 and Fig. 9 with Eqs. (1) and (2), where the boundary between DOX adsorbed and non-adsorbed states is set at *d* equal to 15 Å and the bulk region runs up to 25 Å. The error is calculated by block average. See Section 4.3 for further details and Figs. S8 and S16 for ΔG_a as a function of time.

only consider selected trajectory segments, in which DOX establishes at least one contact with GO, i.e. when DOX is closely approaching or adsorbed on GO. We refer to Section 4.3.1 for methodological details about SOM training and clustering. The trained SOM is depicted in Fig. 6A, where each hexagon represents a neuron corresponding to a set of frames with similar DOX-GO intermolecular distances. Similar neurons are positioned close to each other on the map. Additionally, neurons have been grouped into clusters using hierarchical clustering, indicated by different colors in Fig. 6A. From the population maps in Fig. 6B–D we notice that DOX shares some of the same adsorption modes in the three cases, since most of the neurons, i.e., adsorbed configurations, are partially populated by snapshots from all the three simulations. Therefore, here, we describe all adsorption modes observed and we refer to subsequent subsections for discussion on the effect of group arrangement and GO functionalization (Section 2.3.1 and Section 2.3.2, respectively).

To perform SOM analysis, we must define all possible types of interaction for GO/DOX complex: (i) the hydrophobic and (ii) the π-π stacking interactions of DOX aromatic portion with GO graphitic areas; (iii) the H-bonding of DOX polar groups with GO oxygen-containing groups; and at neutral pH, (iv) the electrostatic interaction of the DOX amino group, which is protonated at both neutral and acidic pH (pK_a = 8.3 [62]), with GO carboxyl groups, which are deprotonated at neutral pH. To obtain information about the characteristics of the adsorbed configurations populating the map we color each neuron according to the average value of specific properties over the configurations belonging to it (Fig. 6E–H). We select two descriptors of the hydrophobic/aromatic part of GO/DOX interaction: 1) the CV *d*, which is basically the distance of the center of mass of DOX aromatic portion from the closest GO carbon atom (Fig. 6E) and 2) the angle, θ, that describes the alignment of the DOX aromatic portion with the average plane of GO (Fig. 6F); and two descriptors of the hydrophilic part of GO/DOX interaction, i.e., 1) the coordination number of DOX protonated amino group by GO oxygen atoms (Fig. 6G) and 2) the number of intermolecular H-bonds established by DOX with GO dot (Fig. 6H). Indeed, there exist several H-bonding scenarios: (i) $–COO^-$ of GO and –OH of DOX; (ii) $–COO^-$ of GO and $–NH_3^+$ of DOX; (iii) –OH of GO and –OH of DOX; (iv) –OH of GO and $–NH_3^+$ of DOX; (v) epoxide of GO and –OH of DOX; and (vi) epoxide of GO and $–NH_3^+$ of DOX.

The left part of Cluster D and few other sparse neurons are characterized by low values of the *d* (3-5 Å) and of the alignment angle, i.e., by a close to parallel alignment (Fig. 6E,F). This means that in these neurons the aromatic anthraquinone portion of DOX interacts through π-π stacking with GO. Interestingly, here we register a low number of H-bonds and a low coordination number for DOX amino group (Fig. 6G,H). Therefore, this adsorption mode has a strong hydrophobic contribution and, according to the *d* value, it corresponds to the first and deepest minimum of the free energy profiles in Fig. 5 (Fig. 6I). As expected, the highest contribution to these neurons comes from the *island* and the functionalized *island* rather than from the *random* GO model (Fig. 6B–D). Indeed, the π-π stacking interaction was experimentally confirmed by the quenching of DOX emission peak at 593 nm in fluorescence spectroscopy, which implies a photoinduced electron-transfer or an efficient energy transfer process in the GO/DOX complex. [27,35]

In Cluster A, B and the right area of cluster D, *d* assumes intermediate values (6-10 Å) and no preferential orientation of the aromatic fragment of DOX is observed (Fig. 6E,F), whereas a higher number of H-bonds is found, especially in Cluster D (Fig. 6H). Indeed, in these adsorption modes, which correspond to the intermediate minimum in Fig. 5, the hydrophilic groups of DOX are more involved, but the aromatic portion of DOX is still quite close to the C backbone of GO in a parallel to oblique orientation. In the central neurons (neurons around 55 and 24) there is also a strong contribution by the DOX amino group (Fig. 6J). The establishment of GO-DOX H-bonds has been experimentally proved by the shift of GO/DOX characteristic FTIR peaks. [27]

Average distance values higher than 10 Å are found mostly in Cluster C, along with intermediate-to-high values of the amino group coordination number and intermediate H-bonds values (Fig. 6E–H). In these adsorption modes, contributing to the shallower minimum in the free energy profiles (Fig. 5), DOX is interacting mainly through its hydrophilic portion, since the distance of the aromatic segment from the C backbone of GO, *d*, is about the size of the molecule (Fig. 6K). This adsorption mode, which should correspond to the third minimum of the free energy profiles, is more common for bare GO dots (Fig. 6B–D).

Overall, two main types of adsorption modes are found with the former analysis: (i) a well-defined lowest energy adsorption mode for DOX – first minimum – is driven by the parallel alignment of the aromatic portion of DOX on top of the graphitic islands of GO, when they are available, and this is present also for PEGylated GO; (ii) a pool of adsorption modes where the electrostatic and the H-bonding GO-DOX interactions play a significant role and these correspond mainly to the two less deep free energy minima and are available in all the three models. Both the aromatic and the polar components of GO/DOX interaction have experimental proofs, as mentioned above. [27,35] Moreover, the fact that the loading and release processes show a strong pH dependence [23,27–29] implies that some pH-sensitive groups of DOX and/or GO must be involved in the adsorption.

The effect of GO functional groups distribution on DOX adsorption is discussed in Section 2.3.1, whereas the effect of GO functionalization with realistic PEG-cRGD chains in Section 2.3.2. Finally, the effect of a decrease in the pH conditions on DOX adsorption is discussed in Section 2.3.3.

2.3.1. Implications of oxidation (in)homogeneity

To understand the effect of different oxygen-containing groups arrangement on DOX adsorption, we compare GO_i and GO_r free energy

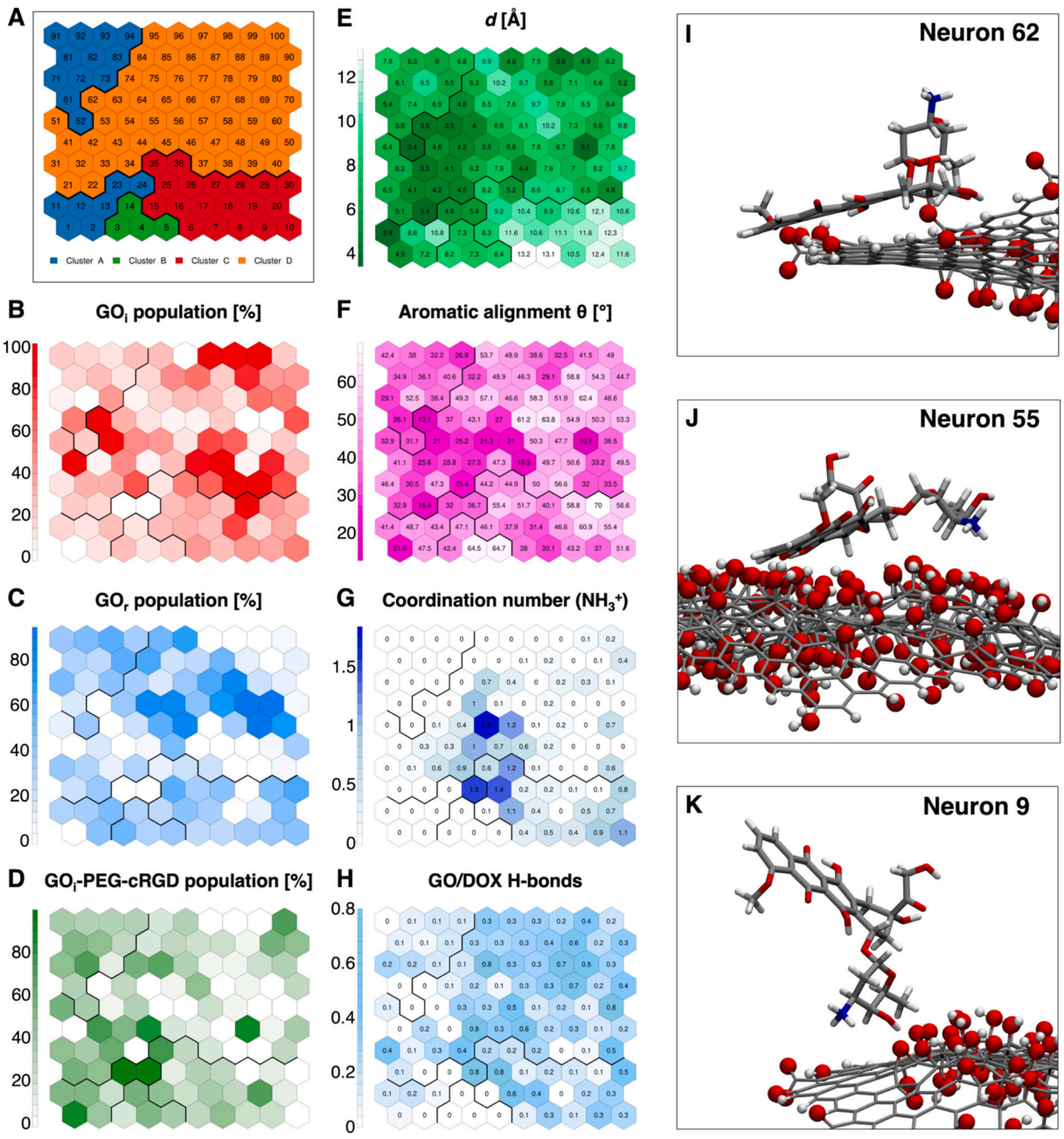

Fig. 6. (A) Trained SOM, with the neurons numbered and colored according to the cluster they belong to. The number of clusters was chosen from the Silhouette profile in Fig. S10. (B,C,D) Population maps for the three systems. (E-H) The SOM where each neuron is colored according to its average value of four GO/DOX descriptors: two descriptors of the hydrophobic/aromatic GO/DOX interaction, i.e., (E) the distance used as the CV during MetaD – that is basically the distance of the center of mass of DOX aromatic portion from the closest GO C atom and (F) the alignment of the DOX aromatic portion with the plane of GO – plane of GO is approximated; two descriptors of the hydrophilic GO/DOX interaction, i.e., (G) the coordination number of DOX protonated amino group and (H) the number of H-bonds established by DOX with GO dot. The details about the analysis can be found in Section 4.3. (J-K) Representative DOX adsorption modes belonging to neuron 62 (GO$_i$), 55 (GO$_r$) and 9 (GO$_i$), respectively.

profiles. We observe a similar shape with a slight shift in the location of the deepest minimum, whereas a significant variation in the depth of each minimum is found. The random oxygen-containing groups arrangement is responsible for decreasing the strength of the adsorption free energy of one DOX molecule by 6.4 kcal mol^{-1}. This gap essentially comes from the reduced accessibility to large unoxidized regions of GO surface along with an increased solvation of the oxidized groups going from GO$_i$ to GO$_r$ (Section 2.1). Therefore, we can say that the π-π stacking interaction, which is only possible when pure graphitic areas are present, plays a crucial role in the loading of DOX on GO. In fact, Don Subasinghege et al., who computationally investigated the adsorption of aniline – an aromatic molecule – on GO sheets with different oxidation levels, found an increase of about 2 kcal mol^{-1} in the adsorption free energy going from a C/O ratio of 4 to a C/O ratio of 2, i.e., a weakening of the GO/aniline interaction upon increasing of GO oxidation level. [63]

To achieve a more thorough comprehension of DOX adsorption modes onto GO$_i$ to GO$_r$, it is interesting to evaluate the free energy dependence on other CVs than the one biased in MetaD simulations (*d*). This is done by reweighting the MetaD simulation, i.e. removing the bias applied along the simulation and computing the free energy surface in terms of any other CV (see Section 4.3 for further details about the

reweighting procedure).

First, we examine the 2D free energy surfaces obtained by reweighting the MetaD simulations with respect to the angle between the hydroxyanthraquinone and GO planes, θ, as the second CV in addition to *d*, the originally biased one (Fig. S11). These surfaces reveal a different free energy landscape for GO_i and GO_r. In both cases, the lowest energy region is located at a short distance *d* from the GO dot. However, deep and more localized minima are found around –180°, 0° and 180° (parallel alignment) for the *island* model, while a broad and shallower minimum, i.e., no preferential orientation of DOX aromatic portion, is observed for the *random* model. Moreover, in Fig. S11, in agreement with the free energy profiles in Fig. 5, we do not find minima at distances higher than 15 Å. The concurrence of a close distance (low *d*) and a parallel relative orientation (low θ) between DOX hydroxyanthraquinone and GO is typical of π-π stacking interaction between two aromatic structures. As we anticipated in the SOM analysis, this happens only for GO_i. Indeed, the neurons sharing low *d* (Fig. 6E) and low θ (Fig. 6F) values are mainly populated by GO_i/DOX adsorption modes rather than GO_r/DOX (Fig. 6B vs 6C). The missing π-π stacking interactions are responsible for the strong deviation of GO_r adsorption free energy profile from GO_i one at low *d* values (Fig. 5).

The complementary contribution to the adsorption are the electrostatic and hydrogen-bonding interactions, which are not only believed to be important for the adsorption, but also responsible for the pH dependence of drug loading/release processes. [29] To examine the role of the positively charged NH_3^+ group in the adsorption, we reweighted the MetaD simulations with respect to the coordination number of DOX protonated amine group by GO oxygen atoms (Fig. S12). For both GO_i and GO_r, there are four minima located at coordination numbers equal to 0, 1, 2 and 3. The minima are very close in energy for GO_i and GO_r and even extend to *d* values of 14 Å from the GO surface. This means that the NH_3^+ group plays a significant role independently from the functional group distribution and also for adsorption modes in which DOX aromatic portion is far from the surface, in agreement with the findings of different adsorption modes from the SOM analysis above. Moreover, we note that the number of simultaneous H-bonds established by DOX is higher for GO_r than for GO_i, as we can see from the relative frequency values in Fig. S13. This is in line with our results of Section 2.1, where we found that the number of H-bonds of GO with the surrounding water molecules is higher for GO_r, whereas GO_i favors intramolecular interactions. From an energetic point of view, we averaged the GO/DOX non-bonded interaction energy over DOX adsorbed states in Table S3. Based on the values in Table S3, we find that the ratio between van der Waals and electrostatic absolute values decreases from about 5:1 to 2:1 going from the *island* to the *random* model. This finding further confirms how the distribution of the oxygen groups impacts on the type of interaction established by the drug molecule with the carrier.

Lastly, to understand how strongly DOX binds to different GO dots regions, we reweight the MetaD simulations with respect to *x*, *y* and *z* coordinates of the center of mass of DOX *C* ring. The free energy maps in Fig. 7 essentially tell how strong the aromatic portion adsorbs (Fig. 7A–D) and at which distance (Fig. 7E–H). For GO_i we notice that the deepest minima are located on the graphitic regions (Fig. 7A,B vs Fig. 1B) and that the free energy in the central oxidized area ranges from –6 to 0 kcal mol^{-1}. We can see a slight difference in the upper and lower surfaces of GO in the adsorption free energy in the central region, which may be due to the different concavity, since the upper surface is convex and the lower surface is concave (Fig. 1B). This might correspond to a slight preference for DOX to adsorb on concave oxidized regions rather than convex ones. For GO_r there is no preferential adsorption site

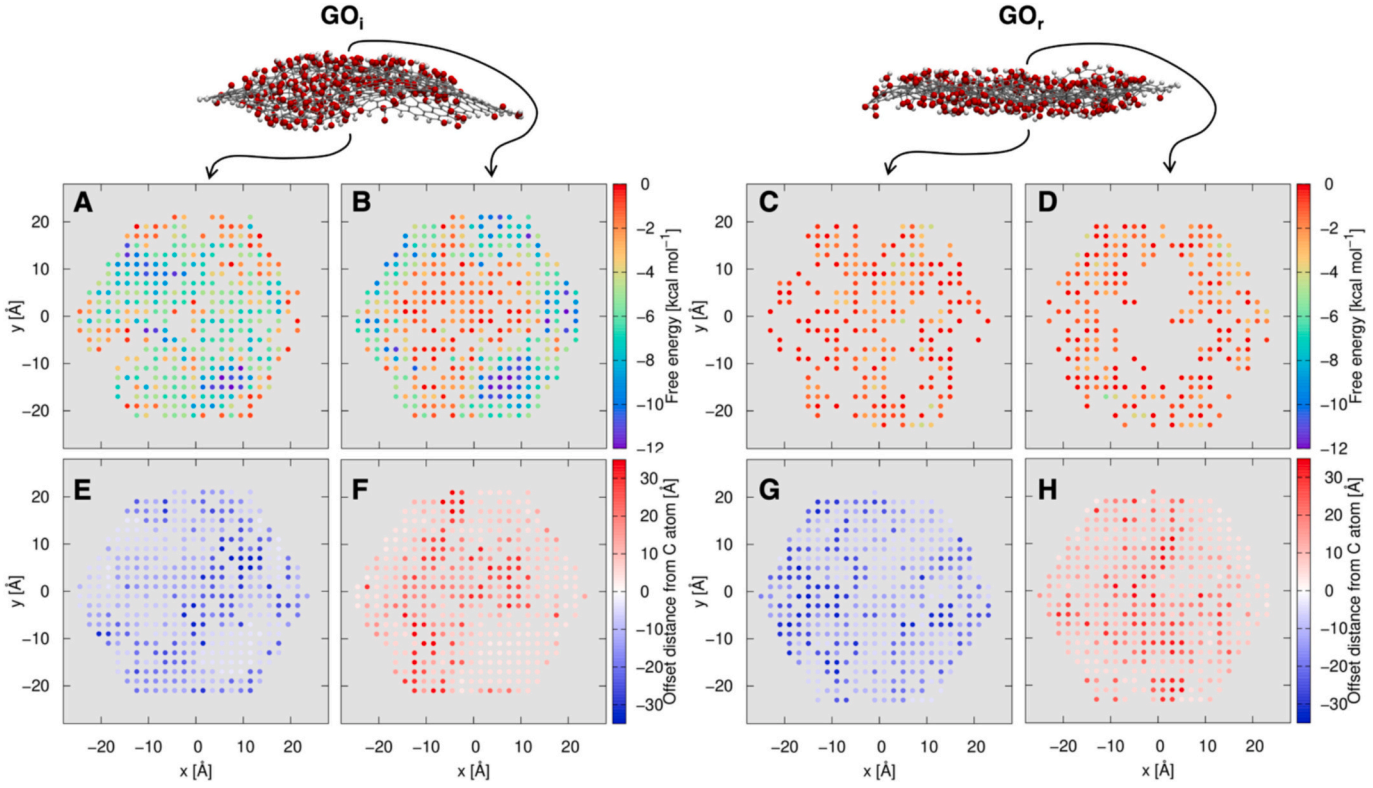

Fig. 7. (A–D) Map of the DOX adsorption free energy values associated with each C atom of the GO surface as obtained by the reweighting of the MetaD simulations against *x*,*y* and *z* coordinates of DOX aromatic portion center of mass, which is essentially located at the center of ring C in Fig. 4A. The minimum free energy value scanning *z* towards positive (top) and negative (bottom) values from the C *z* coordinate was selected and plot in the top (A,C) and bottom (B,D) surfaces for GO_i and of GO_r, respectively. The complementary maps (E-H) indicate the offset distance of each point in the above plots (A-D) with respect to the C atom, which is essentially calculated as the difference of *z* coordinates of (*x*,*y*) point whose free energy is the one in the above plot and of the underlying C atom, i.e. the distance from the GO dot. The same color scales were used in all plots to allow for better comparison.

Table 4
Non-exhaustive collection of DOX loading and release percentage data by GO nanocarriers at different pH values, from literature experimental works. [22,23,25,27,29,64,67–69] Abbreviations are listed below.[a]

Ref.	Carrier (size)[b]	C/O	Loading	Release
Bare GO				
[27]	GO	NA	*pH 2*: 0.55 mg/mg[e] *pH 6*: 0.91 mg/mg[e] *pH 10*: 0.74 mg/mg[e]	*pH 2*: 71 % after 30 h *pH 7*: 11 % after 30 h *pH 10*: 25 % after 30 h
[29]	GO	1.2	*pH 3.4*: 0.91 mg/mg[f] *pH 5.0*: 0.92 mg/mg[f] *pH 7.2*: 0.94 mg/mg[f]	*pH 1.0*: 23 % *pH 3.2*: 6 % *pH 7.0*: 0 %
[64]	GO (10–200 nm)	NA	–	*pH 5.3*: 48 % after 24 h[g,h]
[68]	GO (70–800 nm)	NA	*pH 5.4*: 95 %[g,h] *pH 7.4*: 179 %[g,h] *pH 9.4*: 198 %[g,h]	*pH 5.4*: 81 % after 72 h[g,i] *pH 7.4*: 43 % after 72 h[g,i]
[69]	GO	NA	~1 mg/mg	*pH 5.3*: 36 % after 72 h[g] *pH 7.4*: 12 % after 72 h[g]
Functionalized GO				
[22]	GO-4armPEG$_{2000}$ (141 nm)[c]	NA	0.37 mg/mg	*pH 5.3*: 65 % after 72 h[c,g] *pH 7.4*: 29 % after 72 h[c,g]
[23]	NanoGO-6armPEG (<20 nm)[j]	NA	–	*pH 5.5*: 50 % after 48 h *pH 7.4*: 15 % after 48 h
[25]	GO-hPG (5–30 nm)	NA	12.5 % (*w*/w%)	*pH 5.6*: 19 % after 48 h *pH 7.4*: 14 % after 48 h
[25]	GO-hPG-cR$_{10}$ (5–30 nm)	NA	11.7 % (w/w%)	*pH 5.6*: 20 % after 48 h *pH 7.4*: 13 % after 48 h
[67]	GO-PEI·Ac-FI-PEG-LA[d]	0.75	85 %	*pH 5.8*: 80 % after 72 h *pH 7.4*: 11 % after 72 h
[64]	GO-HA (10–200 nm)	NA	–	*pH 5.3*: 40 % after 24 h[g,h] *pH 5.3*: 40 % after 24 h[g] *pH 7.4*: 20 % after 24 h[g]

[a] Abbreviations: Ac for acetyl group, cR$_{10}$ for cyclic R10 peptide, FI for fluorescein isothiocyanate, HA for hyaluronic acid, hPG for hyperbranched polyglycerol, LA for lactobionic acid, PEG for polyethylene glycol, PEI for polyethyleneimine, NA for not available.
[b] The size always refers to the GO lateral width, when provided.
[c] For dual release of cisplatin (Pt) and DOX.
[d] GO was modified with PEI with terminal groups either derivatized with FI or derivatized with PEG-linked LA or acetylated.
[e] DOX initial concentration of 0.145 mg/mL.
[f] DOX initial concentration of 0.350 mg/mL.
[g] Data collected at 310.15 K (37 °C).
[h] Data collected in phosphate-buffered saline (PBS).
[i] For DOX loaded at pH 7.4.
[j] The size refers to the functionalized GO nanostructures, while PEG MW was not provided.

(Fig. 7C,D) or any concavity/convexity effect, since the GO dot is more homogeneously corrugated (Fig. 1F).

2.3.2. *Implications of functionalization with PEG-cRGD chains*

For the purposes of drug delivery, it is crucial to compare the DOX adsorption feature on GO$_i$-PEG-cRGD with respect to bare GO$_i$ dots. As already mentioned at the beginning of this section, the calculated DOX adsorption free energy to cRGD-conjugated PEGylated *island* GO model is weaker than the one to GO$_i$ (Fig. 5 and Table 3). Interestingly, a decrease in the DOX loading efficiency by GO was also registered experimentally upon GO functionalization with hyaluronic acid and, eventually, RGD. [35] However, according to the SOM analysis, the presence of PEG-cRGD chains does not hamper the DOX from exploring any of the above-mentioned adsorption modes, but eventually influences their relative occupancy. For example, the adsorbed configurations in Cluster D have limited accessibility and the higher energy adsorption mode is scarcely populated on GO$_i$-PEG-cRGD model (Fig. 6B-D). Even so, the presence of PEG-cRGD decreases the strength of DOX adsorption, perhaps because it makes more difficult to access to GO surface for steric hindrance considerations and because not all the surface is available being partially covered by PEG. Indeed, DOX competes with PEG-cRGD chains for the adsorption on GO.

Nevertheless, DOX essentially adsorbs on GO even if PEG-cRGD chains are present, i.e. it does bind to PEG-cRGD chains only (Fig. S14). Also, when DOX is adsorbed on GO it does not affect the distribution of the PEG-cRGD chains around the GO dot, whose number density profile in the presence of DOX (Fig. S14) resembles the one for the unloaded GO$_i$-PEG-cRGD system (Fig. 3C). Thus, a similar PEG distribution and RGD availability is expected.

To place our work in context with the existing experimental literature about loading/releasing DOX on/from GO nanostructures, it is important to note that DOX was successfully loaded on GO functionalized with PEG, [22,23] among other polymers [25,64]. The latter systems were also reported to favor pH-triggered DOX release at acidic pH, which is investigated in the next section.

2.3.3. *Implications of pH decrease*

DOX release from GO-based nanocarriers is generally triggered by acidic pH values, [23,27–29] both for bare GO and PEGylated GO. [6] This effect has great potential, given that acidic pH values (5-6) were registered in tumor microenvironment (TME), [65] which is nanomedical devices target site, and in intracellular endosomes, where the nanocarriers are encapsulated when internalized by receptor-mediated endocytosis. [66] Nevertheless, the driving mechanism of DOX pH-triggered release from GO nanocarriers is still under debate. [23,27,29,67] A collection of the percentage values for DOX loading and release by uncoated and functionalized GO nanocarriers at different pH, as gathered from the experimental literature, is included in Table 4. It is evident that an acidic pH condition (2-5.8) always leads to a greater DOX release with respect to physiological pH condition (~7.4) over the same time frame. Based on these data, the registered ratio between the percentage of DOX released at acidic pH with respect to neutral pH

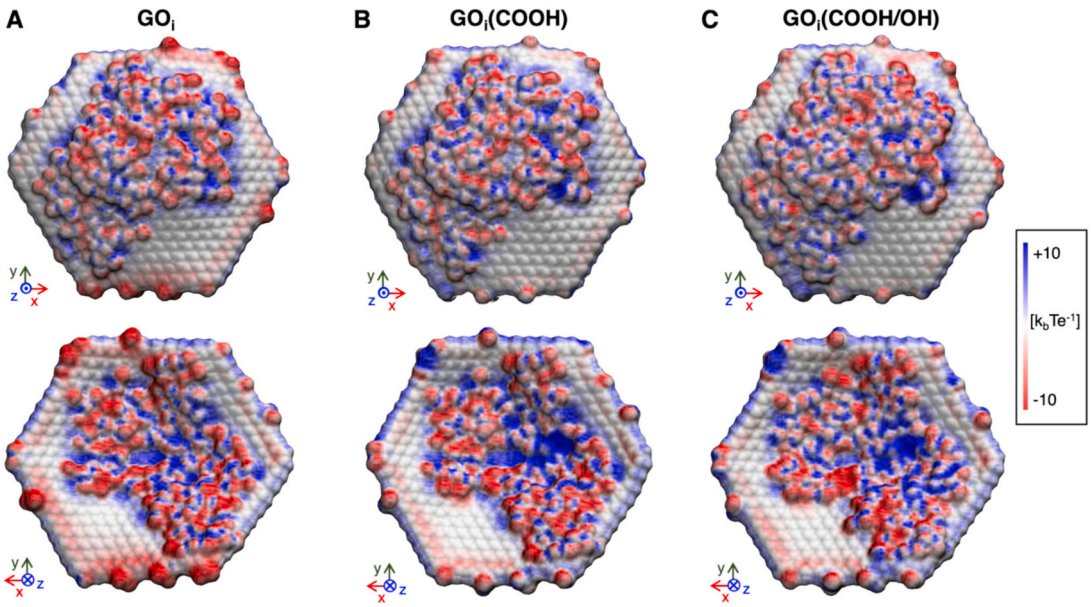

Fig. 8. Visualization of the electrostatic potential on the molecular surface of GO$_i$ dots at pH = 7.4 (A) or pH = 5.5, mimicked only by carboxyl groups protonation (B) or by carboxyl groups protonation and epoxide rings opening (C). The molecular surface was represented by using OPLS-AA atomic radii and a probe radius of 1.4 Å and the electrostatic potential was calculated with the Adaptive Poisson-Boltzmann Solver (APBS) code. Further details on the APBS calculations can be found in Section 4.1.

ranges from 2 to 8. A complete DOX release has never been reported to date, as far as the authors know.

In this context, to investigate pH-triggered DOX release from GO, we have performed two additional MetaD simulations for the realistic nanodevice model GO$_i$-PEG-cRGD (overall charge, q = -4 e; C/O = 2.5). To mimic the TME and endosomal slightly acidic pH value of 5.5, the structure of GO was modified as follows: (i) in GO$_i$(COOH)-PEG-cRGD all the edge carboxyl groups were protonated (q = 0 e; C/O = 2.5); (ii) in GO$_i$(COOH/OH)-PEG-cRGD all the edge carboxyl groups were protonated and simultaneously 30 % of the basal epoxide groups were opened and turned into *anti* diols (q = 0 e; C/O = 2.2). The technical details about these models can be found in Section 4.1 and simulation details in Section 4.3. To visually show the effect of the structural changes adopted to mimic slightly acidic pH values, in Fig. 8 we represented the molecular surface of GO$_i$-PEG-cRGD, GO$_i$(COOH)-PEG-cRGD and GO$_i$(COOH/OH)-PEG-cRGD colored according to the electrostatic potential calculated by solving the Poisson-Boltzmann equation. We note a reduced amount of red spots (negative potential) on the edge of the GO flake both in GO$_i$(COOH)-PEG-cRGD and GO$_i$(COOH/OH)-PEG-cRGD and an increased amount of blue (positive potential) and white (neutral potential) spots on the surface of GO$_i$(COOH/OH)-PEG-cRGD compared to GO$_i$(COOH)-PEG-cRGD, due to the increased number of basal hydroxyl groups.

The system with protonated carboxyl groups (i), which is the common practice to simulate GO in acidic conditions [32,70–74], is herein taken as a reference. Indeed, according to their pK_a value, the edge carboxyl groups are expected to be protonated at slightly acidic pH conditions. [51] Nevertheless, we believe that the pH = 5.5 condition is better reproduced by the system (ii) with both protonated carboxyl groups and 30 % of opened epoxide rings (turned into diols). In fact, it is well known that the epoxide ring opening reaction is catalyzed by acidic aqueous media, where water can directly serve as the nucleophile species. [75,76] Moreover, the epoxide ring opening reaction was observed during ab initio MD simulations of GO systems, even at neutral pH, by at least two independent groups, [43,77] but was never introduced in classical MD simulation models, as far as we know. In both (i) and (ii) systems, the overall charge of the nanocarrier is neutralized, which agrees with the experimentally registered decrease in the absolute value of the zeta potential following a pH decrease. [29,51]

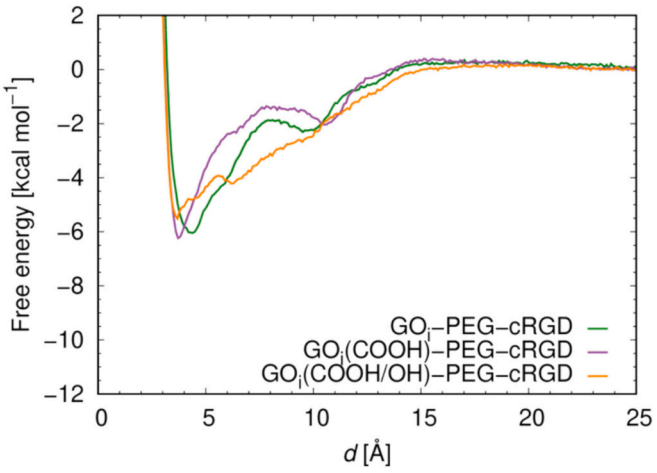

Fig. 9. Free energy profiles of DOX loading on GO$_i$-PEG-cRGD at pH 7.4 (GO$_i$-PEG-cRGD) and pH 5.5 (GO$_i$(COOH)-PEG-cRGD and GO$_i$(COOH/OH)-PEG-cRGD). Increasing values of the distance d correspond to the DOX aromatic portion moving away from the GO surface towards the bulk solution. Each of the profiles is calculated as the average from 800 ns to the end of the simulation time.

Both models (i) and (ii) were used as a substrate for DOX adsorption in two independent MetaD simulations. We first checked that the surface of the GO dot was uniformly sampled by DOX along the MetaD in Fig. S15 and that a good convergence was achieved by estimating the error on the free energy with block analysis in Fig. S16.

We register a decrease in the absolute value of the adsorption free energy ΔG_a in Table 3 by 0.2 kcal mol^{-1} going from GO$_i$-PEG-cRGD to GO$_i$(COOH)-PEG-cRGD, and by 0.4 kcal mol^{-1} going from GO$_i$-PEG-cRGD to GO$_i$(COOH/OH)-PEG-cRGD. This corresponds to a weakening of the interaction between DOX and GO for both MetaD simulations at pH 5.5 with respect to the one at pH 7.4, which agrees with the experimental data on pH-triggered DOX release mechanism mentioned above.

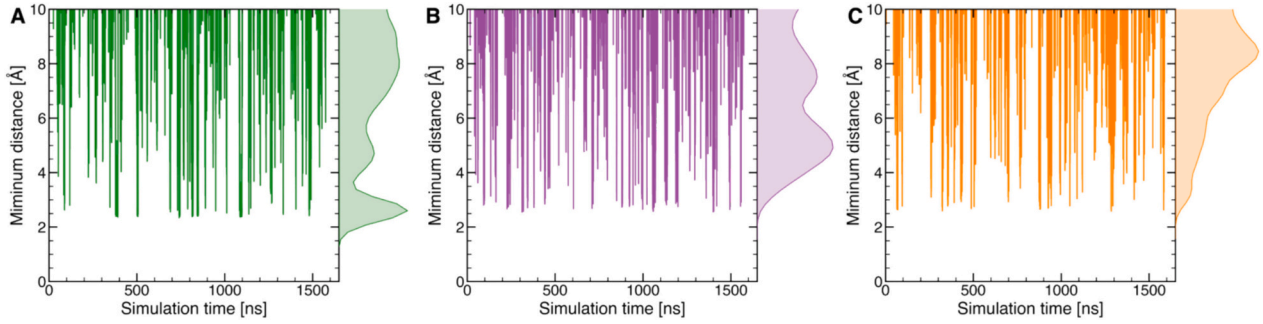

Fig. 10. Time evolution and reweighted histograms (calculated by kernel density estimate) of the minimum distance between the protonated N atom of DOX and the carboxyl O atoms of GO computed along (A) GO_i-PEG-cRGD, (B) GO_i(COOH)-PEG-cRGD and (C) GO_i(COOH/OH)-PEG-cRGD MetaD simulations.

Nevertheless, the average ΔG_a values take into account all the various adsorbed states sampled in our MetaD simulations, for d values within the range 0-15 Å in Fig. 9. To understand which of the molecular interactions is more affected, we performed further analyses.

By looking at the histograms of the minimum distance values between the protonated N atom of DOX and the carboxyl O atoms of GO in Fig. 10, we can state that the protonation of the carboxyl groups strongly affects the DOX adsorption. Given that 99 % of the cases in which the minimum N—O distance is within 3.5 Å falls in the deepest free energy minimum (i.e., the minimum distance is below 3.5 Å and simultaneously d is in the range 0-7.5 Å), we believe that the loss of this interaction at slightly acidic pH is responsible for the changes observed in the global minimum of the free energy profiles in Fig. 9. Indeed, the protonation of GO edge carboxyl groups implies both the loss of excellent H-bond acceptor groups and the shift from a negatively charged carrier to a neutral one, which are detrimental for the positively charged DOX molecule. Moreover, we note that a lower number of H-bonds is established between DOX and GO at pH 5.5 than at pH 7.4, on average, in the adsorbed states ($d < 15$ Å), in Fig. S13. Lastly, in Fig. 9 the shape of the average free energy profile of GO_i(COOH/OH)-PEG-cRGD/DOX presents different features than GO_i-PEG-cRGD/DOX and GO_i(COOH)-PEG-cRGD/DOX. This might be related both to the different GO/DOX and GO/PEG interactions, upon increasing the number of the basal hydroxyl groups on GO. By collecting the average number of contacts (Fig. S17) between various components of the system for the DOX adsorbed states ($d < 15$ Å) in Table S4, we note that PEG-cRGD chains are interacting more with DOX in GO_i(COOH/OH)-PEG-cRGD/DOX than in all other cases.

To conclude on the pH decrease effect, the ΔG_a values estimated by MetaD simulations at pH 7.4 and 5.5 correctly reproduce the trend expected from experimental data. According to the Boltzmann distribution, the difference between the adsorption free energy values for DOX on GO_i-PEG-cRGD and GO_i(COOH/OH)-PEG-cRGD, i.e. at neutral or acidic pH, corresponds to a 2-fold increase in the probability of finding DOX in the solvent under acidic conditions. We cannot exclude that other additional effects play a complementary role in the release process. One could be related to the DOX concentration. We must point out that the experimental GO loading capacity of 1.43 mg/mg [29] corresponds to the simultaneous adsorption of almost 30 DOX molecules on a GO dot of the size of the one used in this work according to the various adsorption modes found in this work and even interacting among themselves.

3. Conclusions

In this study, we successfully built two types of models of bare and coated graphene oxide dots: (i) the more realistic *island* models, in which highly oxidized areas coexist with graphitic unoxidized regions and (ii) the *random* models, which feature a homogeneous arrangement of GO functional groups.

We found that the water solvation of oxygen-containing groups is reduced in *island* GO dot, in favor of a higher content of intramolecular H-bonds, with respect to the *random* one. We observed that PEGylation of both GO dots – at a grafting density similar to the experimental values – does not lead to a complete sheltering of GO surface, yet to a partial coverage of both graphitic and oxidized areas. The conjugation with a cyclic RGD targeting ligand does not affect the system behavior since the targeting ligand is highly solvated.

As a next step, to achieve a deep atomistic and quantitative understanding of DOX adsorption modes on bare *island* and *random* GO dots and on cRGD-conjugated PEGylated *island* GO dots, we used MetaD method for an enhanced sampling of adsorption events. We found several configurations involving different sites, which can be grouped into three main categories, according to the DOX orientation with respect to the GO plane and based on the key interactions: (i) the most thermodynamically stable mode in which DOX aromatic portion aligns with GO surface and interacts mainly with aromatic/hydrophobic interactions, (ii) the second most thermodynamically stable mode in which DOX hydrophilic portion also plays a significant role establishing hydrogen-bonding and electrostatic interactions, (iii) the least thermodynamically stable mode in which the aromatic portion points towards the solvent and DOX scarcely interacts with GO surface through its hydrophilic portion.

Based on our calculations, two important facts emerge: 1) PEGylation does not significantly alter the availability of DOX adsorption modes but causes a reduction of the adsorption free energy, as a consequence of the competition between DOX and PEG for the adsorption on GO surface; 2) when GO is homogeneously oxidized (*random* GO), the most stable adsorption mode (π-π stacking) becomes rare and less stable with respect to the *island* model and DOX mostly binds through electrostatic and H-bond interactions.

As far as the effect of a change towards acidic pH conditions on the GO/DOX affinity, we investigated two modified models, where the carboxylate groups at the GO edges were protonated back to carboxylic acids and, further, some epoxide rings on the surface were opened to diols. Indeed, in both cases the free energy of adsorption is computed to be reduced, facilitating and accelerating the DOX release, in line with a pH-triggered release mechanism.

Therefore, our findings allow to outline the features of the ideal graphene-based DOX carrier, which is highly oxidized, PEGylated GO decorated with cRGD targeting ligands. The pH-triggered drug release is expected to be enhanced for several reasons: 1) high extent of oxidation reduces the graphitic regions on the surface, avoiding the strong DOX adsorption by π-π stacking that would not be triggered by pH-change and would excessively stabilize DOX, while favoring electrostatic interactions and H-bonds; 2) PEGylation improves biocompatibility and in-vivo circulation time but does not affect DOX adsorption on GO; 3) cRGD is also not detrimental for DOX loading but will improve selectivity for the target site.

To conclude, we believe that our study does not only provide an

advancement in the atomistic understanding of drug loading on graphene-based systems, but also important insights into the influence of the oxidation pattern and of a realistic PEG coating for experimentalists to design effective controlled drug release strategies. From a theoretical perspective, the MetaD protocol employed in this study could be utilized to investigate the adsorption of other clinically relevant drug molecules on graphene oxide.

4. Methods

4.1. Building the models of bare and functionalized GO dots

To build bare GO flake-shaped models we made use of MakeGraphitics library [42], which includes a random forest model that oxidizes graphene according to the high correlation between oxidation loci found by Yang et al. [11]. The groups added on graphene are hydroxyl and epoxy groups on the basal plane and phenol hydroxyl and carboxyl groups on the edges. We built two GO models differing *only* in the way oxygen groups are arranged: an *island* model (GO_i) with hydroxyl and epoxide groups concentrated in oxidized "islands" along with graphitic regions, and a *random* model (GO_r), in which the same number of groups is randomly placed on the surface. To achieve this, we ran carboxyl_ions_with_counterions.py script with two different values for new_island_freq parameter, which is the frequency at which new oxidized islands are initiated. The default 10^{14} value was used for GO_i and 10^{28} for GO_r. Moreover, we assured that the ratio between the number of oxygen groups on each side of the flake is close to one and we run the script enough times to get the same chemical composition and functional groups type and number for GO_i and GO_r. After running the script, we manually added hydroxyl groups on unstable sp^2- hybridized carbon atoms surrounded by only sp^3-hybridized C. The parameters used to run the program are listed in Table S5, whereas the characteristics of the models in Table 5 and Table S6. Our models differentiate from the common Lerf- Klinowski model, [78] which is the most widely used in computational GO works and contains only hydroxyl, epoxide and carboxyl groups *randomly* arranged on the surface.

Both *island* and *random* models share the same diameter of 50 Å, non-stoichiometric structural formula of $C_{2.5}O_1H_{0.8}$, [10] and the same C/O ratio of 2.5, which is a common value for GO synthetized with the modified Hummers' method [7] that is widely used for GO biomedical applications. [23,27,33,54,64,68] Moreover, the ratio between the groups on the edges and on the basal plane of the GO dot (edge/basal ratio in Table 5), agrees with the values found in Ref. [79] The protonation of the carboxyl groups at the edges of the GO dot was set according to their pK_a values [51] with Henderson-Hasselbach equation for physiological pH (7.4), which predicts that 6 out of 7 COOH are in their deprotonated state. [51] This results in a charge density of −51C g^{-1} in agreement with the experimental one [51] and with GO negative zeta potential values. [29] In the first column of Fig. 1 the structures of *island* and *random* bare GO models are represented with atoms colored according to the type of group they belong to.

Subsequently, both bare GO models were functionalized with four NH_2-PEG_{1000}-COO^- chains to provide them with stealth properties or with four NH_2-PEG_{1000}-cRGD chains to provide them also with active targeting ligands. PEG_{1000} is a polyethylene glycol chain composed of 22 monomeric units yielding a molecular weight of approximately 1000 g mol^{-1} and cRGD stands for c(RGDyK), an RGD-based cyclic pentapeptide commonly used for integrin $\alpha_V\beta_3$ targeting. A very similar functionalization pattern was achieved experimentally by Bidram et al. [20] The number of PEG or PEG-cRGD chains corresponds to a weight percentage to 25 % wt and was set to correspond to the upper limit of the weight percentage range reported from the TGA characterization of PEGylated GO (4-25 %) in the experimental works, [20,33,54–56] after normalization by the molecular weight of the PEG chain. Therefore, the model PEG grafting density is consistent with the experimentally achievable one for a system of this size. In particular, two PEG chains are connected to the basal plane, as a result of an epoxide ring opening reaction (Fig. S4A) and the other two are bonded to the edge carboxylic groups from an amidation process (Fig. S4B). This choice allows to obtain a uniform PEGylation of the GO dot and takes into account that the most commonly used technique, i.e., the amidation, is not chemoselective [10] and, therefore, the amine will also produce the epoxide ring opening on the surface. The same couple of functionalization strategies was also considered in the computational work by Alberto Arenas-Blanco et al. [80] The structure and the topology files of PEGylated and cRGD-conjugated PEGylated models were obtained with in-house *python* script.

To investigate pH-triggered DOX release, we have selected the *island* GO-PEG-cRGD model and modified it to mimic the most probable protonation state of ionizable groups at a slightly acidic pH of 5.5. A reference model was built by protonating the edge carboxylic groups, yielding a neutral model referred to as GO_i(COOH)-PEG-cRGD. To represent a more realistic model, in addition to edge carboxylic groups protonation, 30 % of the basal epoxide groups were opened, i.e., 27 epoxide groups that were randomly chosen on the surface and equally distributed on both sides of the GO surface. Each epoxide group was opened by breaking one of the C—O epoxide bonds, protonating the epoxide O atom and adding a new hydroxyl group on the carbon atom which was left with only three bonds on the other side of the GO plane with respect to the original epoxide group, by means of an in-house python script which performs the required modification to structure and topology files. This latter model is called GO_i(COOH/OH)-PEG-cRGD. We note that the COO^- groups of cRGD aspartate residues were not modified because they are fully deprotonated at pH = 5.5 according to their pK_a value (3.71).

The electrostatic potential around GO_i-PEG-cRGD models at different pH was calculated with Adaptive Poisson-Boltzmann Solver (APBS) through the dedicated server https://server.poissonboltzmann.org/. [81] The dielectric constant of the solute molecule was set to 1, the dielectric constant of the solvent to 78.54, the radius of the solvent molecules was set to 1.4 Å for a water-like molecular surface, the ionic strength to 0.15 M with ions of a radius of 2 Å and the temperature was 298.15 K. OPLS-AA charges and radii were used for GO dots atoms. The molecular surface in Fig. 8 was represented with VMD [82] by using a probe radius of 1.4 Å.

Table 5
Characteristics of GO dot models. A complete list can be found in Table S6.

Dot diameter [Å]	50
Atoms	1037
Mass [g mol^{-1}]	11,367
C/O ratio	2.5
H/O ratio	0.80
Hydroxyl groups	140
Epoxy groups	89
Carboxyl groups	7
Edge/basal ratio	0.06

4.2. Unbiased MD simulations

GO models and liquid water were described using the OPLS-AA force field [83] and the TIP4P water model, [84] respectively. This is a common FF combination for solvated GO [70,85–88] and it was reported to reproduce conformational and hydration energetics of hydrocarbons from electronic structure theory calculations. [83] The GO atom types and parameters are reported in Table S7. The GO dot parameters were assigned by MakeGraphitics library [42] in the LAMMPS topology format, which we converted into the GROMACS with an in-house *python* script. For PEG-COO^-, PEG-cRGD and DOX molecules we used LigParGen [89–91] to assign the OPLS-AA force field parameters and calculate the partial atomic charges according to CM1A charge

model.

The bare or functionalized GO dots were put in cubic boxes of water molecules using GROMACS preparation tools [92] ($80 \times 80 \times 80$ Å^3, $130 \times 130 \times 130$ Å^3 and $140 \times 140 \times 140$ Å^3 sized boxes for $GO_{i/r}$, $GO_{i/r}$-PEG and $GO_{i/r}$-PEG-cRGD, respectively). The appropriate number of Na^+ and Cl^- ions were added to neutralize the system charge and mimic the physiological concentration of 0.15 M. Each of the six systems was minimized with steepest descent algorithm and then heated to 310 K in 2 ns and equilibrated for another 2 ns at constant T and pressure (1 bar). Two replicas of a NPT MD simulation were run for each system, assigning different initial velocities. The V-rescale thermostat [93] with a coupling constant of 1.0 ps and Parrinello-Rahman barostat [94] with a coupling constant of 2.0 ps were used to control temperature (310 K) and pressure (1 bar). We employed LINCS algorithm to constrain the bonds involving H atoms and Newton's equations of motion were integrated with leap-frog algorithm and a timestep of 2.0 fs. Long-range electrostatic interactions were handled with Particle Mesh Ewald method [95] with a cutoff distance of 11 Å, while short-range repulsive and attractive interactions were treated by Lennard-Jones potential with cutoff of 11 Å. Geometric Lennard-Jones combining rules and OPLS-AA [83] 1,4 intra-nonbonded scaling were used. Periodic Boundary Conditions were imposed. All minimization, equilibration, and production steps were performed with open-source GPU-accelerated GROMACS code (version 2022). [92].

We ran 100 ns-long MD simulations for $GO_{i/r}$ and 150 ns-long MD simulations for $GO_{i/r}$-PEG and $GO_{i/r}$-PEG-cRGD. A summarizing table with relevant details of all unbiased MD simulations performed in this work is included in the Supplementary Material (Table S8). The convergence was checked with the trend of solvent accessible surface area and radius of gyration in time (Fig. S5). The last 50 ns of each simulation were considered as the production phase for analyses. The average thickness is the average height of the system in the direction perpendicular to the GO dot plane and was calculated with a *tcl* script in VMD. [82] The Root Mean Squared Displacement (RMSD) was calculated with *gmx rms* taking equilibrated structure as the reference. Root Mean Square Fluctuation (RMSF) was calculated with *gmx rmsf*. Solvent Accessible Surface Area (SASA) was calculated with *gmx sasa*, with van der Waals radii in Ref. [96] and with a probe radius of 1.4 Å. H-bonds were counted with *gmx hbond* according to following geometrical criteria: (1) the distance between the H-bond donor and the H-bond acceptor heavy atoms is less than 3.0 Å; (2) the angle H-donor-acceptor is less than 20°. Non-bonded interaction energies were calculated with *gmx energy* and summing van der Waals and coulombic energy contributions. The radius of gyration of each polymer chain was calculated with *gmx gyrate*. Contacts were counted with *gmx mindist* and a cutoff of 4 Å. VMD was used for structural representations. [82] Radial distribution functions, g(r), were obtained with *gmx rdf* with a bin size of 0.2 Å and the appropriate normalization option. Number density profiles were obtained with *gmx density* after aligning the trajectory so that GO flake is perpendicular to the *z*-axis and positioned in the center of the simulation box. The number density profile for negative *z* values was averaged with its corresponding profile for positive *z* values. When not otherwise stated, the structures in the figures are always taken from the first replica, because the two replicas gave similar results. When results of both replicas are reported, they are referred to as replica (i) and replica (ii).

4.3. Metadynamics simulations

MetaD is an enhanced sampling method based on the introduction of a history-dependent bias potential applied to a small number of suitably chosen collective variables (CVs). To justify the need of MetaD, we first performed 500 ns-long unbiased MD simulations for the *island* or the *random* GO dot in complex with a DOX molecule, with its amino group protonated (pK_a = 8.3 [62]). The same simulation box size used for unbiased simulations of GO dots alone was used and DOX was put at a distance of at least 30 Å from the GO dot. The same force field parameters listed in Section 4.2 were used. LigParGen [89–91] was used to assign the OPLS-AA force field parameters and calculate the partial atomic charges according to CM1A charge model for protonated DOX molecule. The same simulation protocols described in Section 4.2 were employed. In particular, we ran three simulations starting from different GO/DOX relative orientations or with different restraint treatment applied to the GO flake for *island* GO/DOX and one simulation *random* GO/DOX. Relevant details of these simulations are included in Table S8. We observed that DOX readily adsorbed on one site of the GO dot and does not diffuse to different regions within the simulation time (please see Fig. S7).

In this work, for MetaD simulations, both *island* and *random* GO dots and cRGD-conjugated PEGylated *island* GO dot equilibrated structures were put in rhombic dodecahedral boxes with boundaries set at 20 Å (bare GO) and 25 Å (functionalized GO) from the solute using the GROMACS preparation tools. [92] One protonated DOX molecule was put at a distance of at least 30 Å from GO dot. The box was filled with water molecules at the experimental bulk water density and the appropriate number of Na^+ and Cl^- ions were added to neutralize the GO charge and mimic the physiological concentration of 0.15 M. The same force field parameters listed in Section 4.2 for GO dots and above for DOX were used. The three systems were minimized with steepest descent algorithm and equilibrated for 2 ns at 310 K and for another 2 ns at 310 K and 1 bar. Then, we set up MetaD simulations according to the protocol already evaluated by our group and originally applied to the case of DOX loading on a TETT-functionalized TiO_2 NP. [49,97] We performed standard MetaD, biasing the distance *d* between the center of mass of DOX ring C and the closest C atom of the GO dot (Fig. 4A), which was calculated with the command DISTANCE and option LOWEST, and imposed a restraint on the GO dot C atoms at the equilibrated structure with a force constant of 10,000 kJ mol^{-1} nm^{-2}. Indeed, ring C is the central ring of the aromatic hydroxyanthraquinone of DOX, which is meant to drive the hydrophobic interaction with GO. [30] We are aware that the chosen collective variable does not describe either the relative position or the relative orientation of the drug with respect to the flake. This type of description would require at least two additional CVs, which would make the MetaD run inefficient – fewer adsorption events would happen in the same simulation time – and slow to converge, as we proved in our previous work, [49] where we showed that biasing only the drug-carrier distance gave the best outcome in terms of convergence and accuracy. In all the MetaD simulations, we used a height of the gaussian hills of 0.5 kJ mol^{-1} with a pace of deposition of 3 ps. The width of the gaussian hills was set to about a half of the standard deviation of *d* during the unbiased MD simulations mentioned earlier in this section. An upper wall (command UPPER_WALLS) at a *d* value of 30 Å and 35 Å was applied for the bare and functionalized GO dot simulations, respectively. Similar parameters were used in our previous work. [49] MetaD simulations were run in the NPT ensemble at 310 K and 1 bar, which were kept constant by the same thermostat and barostat used in unbiased MD simulations, with the same related parameters. The same setup and protocol used for cRGD-conjugated PEGylated island GO at pH 7.4 was also adopted for the two models of cRGD-conjugated PEGylated *island* GO at pH 5.5, GO_i(COOH)-PEG-cRGD and GO_i(COOH/OH)-PEG-cRGD. All MetaD simulations were run with GPU-accelerated GROMACS code (version 2022) [92] and the open-source, community-developed PLUMED library, [98] version 2.8. [99] A summarizing table with relevant details of all MetaD simulations performed in this work is included in the Supplementary Material (Table S9).

The free energy profiles in Figs. 5 and 9 were obtained with *sum_hills* tool as the average free energy profile from 800 ns to the end of the simulation. The profiles have been scaled so that the free energy value in the plateau region, corresponding to non-adsorbed states, equals to 0 kcal mol^{-1}.

The DOX adsorption free energy values, ΔG_a, in Table 3 correspond

to the average of the values shown in Figs. S8 and S16 in the time range from 800 ns to the end of each MetaD simulation. Each ΔG_a value, along the MetaD simulation, was calculated as

$$\Delta G_a = -k_B T \ln K_a \quad (1)$$

where k_B is the Boltzmann constant, T is the temperature, K_a is the adsorption equilibrium constant. The adsorption equilibrium constant K_a was, in turn, calculated with a Boltzmann-weighted summation approach that integrates the free energy landscape obtained by the *sum_hills* tool as

$$K_a = \frac{\sum_{d=0\ \text{Å}}^{15\ \text{Å}} exp\left[-\frac{G_d - G^*_{mean}}{k_B T} \bullet bin_d\right]}{n_{G^*_{mean}} \bullet bin_d} \quad (2)$$

where G_d is the value of the free energy at distance d and the summation runs from $d = 0$ Å to the boundary between adsorbed and non-adsorbed (solvated) DOX states (15 Å), G^*_{mean} is the reference free energy for the non-adsorbed states, calculated as the mean free energy value in the range d = 15-25 Å, bin_d is the bin size for d (1 Å) and $n_{G^*_{mean}}$ is the number of values used to calculate G^*_{mean}. The d values farther than 25 Å are neglected to avoid any spurious effect coming from the wall set at 30 Å or 35 Å. The above procedure was made possible with as in-house python script. Since the drug adsorbed on different regions of the GO flake during MetaD – as it is shown in Fig. 4 – we consider the free energy estimates ΔG_a as the average of the different adsorption modes, which could all be sampled experimentally in the presence of a much higher number of DOX molecules per GO dot. The convergence of the simulations was assessed by monitoring the trend of the adsorption free energy running average and estimating the error on the estimated free energy surface with block average (Fig. S8 and S16).

PLUMED library was also used to unbias and reweight the simulation with other CVs which were not initially biased:

(i) the torsional angle θ defined in Fig. S11, which approximately describes the orientation of the DOX molecule with respect to GO average plane (command TORSION);
(ii) the coordination number between DOX protonated amino group and O atoms of GO (command COORDINATION with R_0 = 4.0 Å, D_0 = 0, NN = 100, and MM = 200 for the associated rational switching function);
(iii) the *x,y,z* coordinates of DOX ring C in Fig. 4A (command POSITION). From the 4-dimensional free energy surface reweighted on *x, y* and *z* values, the minimum energy points moving away along *z* – up and down the GO dot – from each C atom of GO were selected, plotted and colored according to their free energy value in Fig. 7. The complementary maps which indicate the z value of each (*x,y*) point, also in Fig. 7, indicate at which distance the (*x,y*) point, i.e., ring C of DOX, is from the GO dot.

In all cases, the MetaD simulation was post-processed to calculate the additional collective variable(s) along the trajectory, then REWEIGHT_BIAS command was employed to calculate weights that negate the effect of both MetaD and upper wall biases, according to an umbrella-sampling-like reweighting approach. [100] Finally, HISTOGRAM command was used to obtain the free energy surfaces and maps in Figs. 7, S11, and S12. In-house python scripts were used to calculate and plot the H-bonds reweighted frequency in Fig. S13 and the distance in Fig. 10, which was calculated with *gmx mindist* tool. All the other analyses were performed as detailed in Section 4.2. To identify and classify DOX adsorption modes among different MetaD simulations, a SOM was trained as in Section 4.3.1.

4.3.1. SOM

For the characterization of DOX adsorption modes to GO surface we used the *PathDetect-SOM* tool [101] based on the kohonen package. [102,103] *PathDetect-SOM* was originally developed to cluster ligand/protein adsorption events and reconstruct their pathways sampled along single or multiple simulations, and recently used also for other types of interactions, such as nanodevice/target and drug/carrier ones. [49,104,105] The tool performs two tasks: (i) training of a SOM (Self-Organizing Map), which is an unsupervised learning method, [106] with a chosen set of ligand–protein intermolecular distances as input features and assignment of each simulation frame to a neuron on the map, which represents a ligand/protein configurational microstate; (ii) clustering of the neurons by agglomerative hierarchical clustering with complete linkage and Euclidean distance. A 10 × 10 sheet-shaped SOM with a hexagonal lattice shape and without periodicity across the boundaries was trained using 40 DOX-GO intermolecular distances computed only for the frames in which at least one GO-DOX contact occurs (cutoff of 4 Å) along the three MetaD simulations (frames every 150 ps were considered). The latter ones are the distances between DOX N, C and O atoms highlighted in Fig. S9 (atom 3, 10a, O(14), O(4*), N(3*)) and its four closest GO oxygen atoms and its four closest GO carbon atoms. The choice of the closest atoms instead of specific atom allows to account for DOX exploring different areas on both GO planes and edges. This set of distances was chosen to obtain a good description of the interaction of both the anthraquinone ring and the sugar ring of DOX with GO. The optimal number of clusters for neurons clustering was selected as the one corresponding to the second maximum of the Silhouette profile (Fig. S10).

CRediT authorship contribution statement

Giulia Frigerio: Writing – original draft, Visualization, Investigation, Formal analysis, Data curation, Conceptualization. **Stefano Motta:** Writing – review & editing, Methodology, Formal analysis. **Paulo Siani:** Writing – review & editing, Formal analysis. **Edoardo Donadoni:** Writing – review & editing, Formal analysis. **Cristiana Di Valentin:** Writing – review & editing, Supervision, Resources, Project administration, Funding acquisition, Conceptualization.

Declaration of competing interest

The authors declare no conflict of interest.

Data availability

The authors declare that all data generated or analyzed during this study are included in the main text and supplementary figures and tables. The data supporting the findings of this study are available from the corresponding author upon reasonable request.

Acknowledgments

The authors are grateful to Lorenzo Ferraro for his technical support and to Daniele Perilli, Enrico Bianchetti and Omar Abou El Kheir for useful discussion. The research leading to these results has received funding from the European Union – NextGenerationEU through the Italian Ministry of University and Research under PNRR – M4C2-I1.3 Project PE_00000019 "HEAL ITALIA" to Prof. Cristiana Di Valentin CUP H43C22000830006 of the University of Milano-Bicocca.

Appendix A. Supplementary data

Supplementary data to this article can be found online at https://doi.org/10.1016/j.jconrel.2025.01.020.

References

[1] P. Mi, H. Cabral, K. Kataoka, Ligand-installed nanocarriers toward precision therapy, Adv. Mater. 32 (2020), https://doi.org/10.1002/adma.201902604.

[2] J. Ouyang, S. Rao, R. Liu, L. Wang, W. Chen, W. Tao, N. Kong, 2D materials-based nanomedicine: from discovery to applications, Adv. Drug Deliv. Rev. 185 (2022) 114268, https://doi.org/10.1016/j.addr.2022.114268.

[3] P. Siani, S. Motta, L. Ferraro, A.O. Dohn, C. Di Valentin, Dopamine-decorated TiO_2 nanoparticles in water: a QM/MM vs an MM description, J. Chem. Theory Comput. 16 (2020) 6560–6574, https://doi.org/10.1021/acs.jctc.0c00483.

[4] H. Liu, P. Siani, E. Bianchetti, J. Zhao, C. Di Valentin, Multiscale simulations of the hydration shells surrounding spherical Fe3O4 nanoparticles and effect on magnetic properties, Nanoscale 13 (2021) 9293–9302, https://doi.org/10.1039/D1NR01014J.

[5] N. Karki, H. Tiwari, C. Tewari, A. Rana, N. Pandey, S. Basak, N.G. Sahoo, Functionalized graphene oxide as a vehicle for targeted drug delivery and bioimaging applications, J. Mater. Chem. B 8 (2020) 8116–8148, https://doi.org/10.1039/D0TB01149E.

[6] H. Sharma, S. Mondal, Functionalized graphene oxide for chemotherapeutic drug delivery and cancer treatment: a promising material in nanomedicine, Int. J. Mol. Sci. 21 (2020) 6280, https://doi.org/10.3390/ijms21176280.

[7] D.C. Marcano, D.V. Kosynkin, J.M. Berlin, A. Sinitskii, Z. Sun, A. Slesarev, L. B. Alemany, W. Lu, J.M. Tour, Improved synthesis of graphene oxide, ACS Nano 4 (2010) 4806–4814, https://doi.org/10.1021/nn1006368.

[8] M. Wei, T. Lu, Z. Nong, G. Li, X. Pan, Y. Wei, Y. Yang, N. Wu, J. Huang, M. Pan, X. Li, F. Meng, Reductive response and RGD targeting nano-graphene oxide drug delivery system, J. Drug Deliv. Sci. Technol. 53 (2019) 101202, https://doi.org/10.1016/j.jddst.2019.101202.

[9] O. Akhavan, E. Ghaderi, Graphene nanomesh promises extremely efficient in vivo photothermal therapy, Small 9 (2013) 3593–3601, https://doi.org/10.1002/smll.201203106.

[10] S. Guo, S. Garaj, A. Bianco, C. Ménard-Moyon, Controlling covalent chemistry on graphene oxide, Nat. Rev. Phys. 4 (2022) 247–262, https://doi.org/10.1038/s42254-022-00422-w.

[11] J. Yang, G. Shi, Y. Tu, H. Fang, High correlation between oxidation loci on graphene oxide, Angew. Chem. 126 (2014) 10354–10358, https://doi.org/10.1002/ANGE.201404144.

[12] S. Freddi, D. Perilli, L. Vaghi, M. Monti, A. Papagni, C. Di Valentin, L. Sangaletti, Pushing down the limit of NH_3 detection of graphene-based Chemiresistive sensors through functionalization by thermally activated tetrazoles dimerization, ACS Nano 16 (2022) 10456–10469, https://doi.org/10.1021/acsnano.2c01095.

[13] S.S. An, S.-Y. Wu, J. Hulme, Current applications of graphene oxide in nanomedicine, Int. J. Nanomedicine 10 (2015) 9, https://doi.org/10.2147/IJN.S88285.

[14] S.S. Sekhon, P. Kaur, Y.-H. Kim, S.S. Sekhon, 2D graphene oxide–aptamer conjugate materials for cancer diagnosis, NPJ 2D, Mater. Appl. 5 (2021) 21, https://doi.org/10.1038/s41699-021-00202-7.

[15] M. Papi, V. Palmieri, L. Digiacomo, F. Giulimondi, S. Palchetti, G. Ciasca, G. Perini, D. Caputo, M.C. Cartillone, C. Cascone, R. Coppola, A.L. Capriotti, A. Laganà, D. Pozzi, G. Caracciolo, Converting the personalized biomolecular corona of graphene oxide nanoflakes into a high-throughput diagnostic test for early cancer detection, Nanoscale 11 (2019) 15339–15346, https://doi.org/10.1039/C9NR01413F.

[16] M. Sopotnik, A. Leonardi, I. Križaj, P. Dušak, D. Makovec, T. Mesarič, N.P. Ulrih, I. Junkar, K. Sepčić, D. Drobne, Comparative study of serum protein binding to three different carbon-based nanomaterials, Carbon N. Y. 95 (2015) 560–572, https://doi.org/10.1016/j.carbon.2015.08.018.

[17] M. Li, X. Yang, J. Ren, K. Qu, X. Qu, Using graphene oxide high near-infrared absorbance for photothermal treatment of Alzheimer's disease, Adv. Mater. 24 (2012) 1722–1728, https://doi.org/10.1002/adma.201104864.

[18] B. Wang, H. Guo, H. Xu, Y. Chen, G. Zhao, H. Yu, The role of graphene oxide nanocarriers in treating gliomas, Front. Oncol. 12 (2022) 176, https://doi.org/10.3389/fonc.2022.736177.

[19] G. Liu, H. Shen, J. Mao, L. Zhang, Z. Jiang, T. Sun, Q. Lan, Z. Zhang, Transferrin modified graphene oxide for glioma-targeted drug delivery: in vitro and in vivo evaluations, ACS Appl. Mater. Interfaces 5 (2013) 6909–6914, https://doi.org/10.1021/am402128s.

[20] E. Bidram, A. Sulistio, H.J. Cho, A. Amini, T. Harris, A. Zarrabi, G. Qiao, A. Stewart, D.E. Dunstan, Targeted graphene oxide networks: cytotoxicity and synergy with anticancer agents, ACS Appl. Mater. Interfaces 10 (2018) 43523–43532, https://doi.org/10.1021/acsami.8b17531.

[21] A. Boddu, S.R. Obireddy, D. Zhang, K.S.V.K. Rao, W.-F. Lai, ROS-generating, pH-responsive and highly tunable reduced graphene oxide-embedded microbeads showing intrinsic anticancer properties and multi-drug co-delivery capacity for combination cancer therapy, Drug Deliv. 29 (2022) 2481–2490, https://doi.org/10.1080/10717544.2022.2100512.

[22] X. Pei, Z. Zhu, Z. Gan, J. Chen, X. Zhang, X. Cheng, Q. Wan, J. Wang, PEGylated nano-graphene oxide as a nanocarrier for delivering mixed anticancer drugs to improve anticancer activity, Sci. Rep. 10 (1) (2020) 1–15, https://doi.org/10.1038/s41598-020-59624-w.

[23] X. Sun, Z. Liu, K. Welsher, J.T. Robinson, A. Goodwin, S. Zaric, H. Dai, Nano-graphene oxide for cellular imaging and drug delivery, Nano Res. 1 (2008) 203–212, https://doi.org/10.1007/s12274-008-8021-8.

[24] E. Quagliarini, R. Di Santo, D. Pozzi, P. Tentori, F. Cardarelli, G. Caracciolo, Mechanistic insights into the release of doxorubicin from graphene oxide in cancer cells, Nanomaterials 10 (2020) 1482, https://doi.org/10.3390/NANO10081482.

[25] Z. Tu, I.S. Donskyi, H. Qiao, Z. Zhu, W.E.S. Unger, C.P.R. Hackenberger, W. Chen, M. Adeli, R. Haag, Graphene oxide-cyclic R10 peptide nuclear translocation nanoplatforms for the surmounting of multiple-drug resistance, Adv. Funct. Mater. 30 (2020) 2000933, https://doi.org/10.1002/adfm.202000933.

[26] W. Miao, G. Shim, S. Lee, S. Lee, Y.S. Choe, Y.K. Oh, Safety and tumor tissue accumulation of pegylated graphene oxide nanosheets for co-delivery of anticancer drug and photosensitizer, Biomaterials 34 (2013) 3402–3410, https://doi.org/10.1016/J.BIOMATERIALS.2013.01.010.

[27] X. Yang, X. Zhang, Z. Liu, Y. Ma, Y. Huang, Y. Chen, High-efficiency loading and controlled release of doxorubicin hydrochloride on graphene oxide, J. Phys. Chem. C 112 (2008) 17554–17558, https://doi.org/10.1021/jp806751k.

[28] E. Khakpour, S. Salehi, S.M. Naghib, S. Ghorbanzadeh, W. Zhang, Graphene-based nanomaterials for stimuli-sensitive controlled delivery of therapeutic molecules, Front. Bioeng. Biotechnol. 11 (2023) 1129768, https://doi.org/10.3389/fbioe.2023.1129768.

[29] S. Wu, X. Zhao, Y. Li, Q. Du, J. Sun, Y. Wang, X. Wang, Y. Xia, Z. Wang, L. Xia, Adsorption properties of doxorubicin hydrochloride onto graphene oxide: equilibrium, kinetic and thermodynamic studies, Materials 6 (2013) 2026–2042, https://doi.org/10.3390/ma6052026.

[30] J.T. Robinson, S.M. Tabakman, Y. Liang, H. Wang, H. Sanchez Casalongue, D. Vinh, H. Dai, Ultrasmall reduced graphene oxide with high near-infrared absorbance for photothermal therapy, J. Am. Chem. Soc. 133 (2011) 6825–6831, https://doi.org/10.1021/ja2010175.

[31] H. Vovusha, D. Banerjee, M.K. Yadav, F. Perrozzi, L. Ottaviano, S. Sanyal, B. Sanyal, Binding characteristics of anticancer drug doxorubicin with two-dimensional graphene and graphene oxide: insights from density functional theory calculations and fluorescence spectroscopy, J. Phys. Chem. C 122 (2018) 21031–21038, https://doi.org/10.1021/acs.jpcc.8b04496.

[32] M. Mahdavi, F. Rahmani, S. Nouranian, Molecular simulation of pH-dependent diffusion, loading, and release of doxorubicin in graphene and graphene oxide drug delivery systems, J. Mater. Chem. B 4 (2016) 7441–7451, https://doi.org/10.1039/C6TB00746E.

[33] Z. Xu, S. Wang, Y. Li, M. Wang, P. Shi, X. Huang, Covalent functionalization of graphene oxide with biocompatible poly(ethylene glycol) for delivery of paclitaxel, ACS Appl. Mater. Interfaces 6 (2014) 17268–17276, https://doi.org/10.1021/am505308f.

[34] Z. Xu, S. Zhu, M. Wang, Y. Li, P. Shi, X. Huang, Delivery of paclitaxel using PEGylated graphene oxide as a nanocarrier, ACS Appl. Mater. Interfaces 7 (2015) 1355–1363, https://doi.org/10.1021/am507798d.

[35] Y. Guo, H. Xu, Y. Li, F. Wu, Y. Li, Y. Bao, X. Yan, Z. Huang, P. Xu, Hyaluronic acid and Arg-Gly-Asp peptide modified graphene oxide with dual receptor-targeting function for cancer therapy, J. Biomater. Appl. 32 (2017) 54–65, https://doi.org/10.1177/0885328217712110.

[36] N. Luo, D. Ni, H. Yue, W. Wei, G. Ma, Surface-engineered graphene navigate divergent biological outcomes toward macrophages, ACS Appl. Mater. Interfaces 7 (2015) 5239–5247, https://doi.org/10.1021/am5084607.

[37] M. Mahdavi, A. Fattahi, E. Tajkhorshid, S. Nouranian, Molecular insights into the loading and dynamics of doxorubicin on PEGylated graphene oxide nanocarriers, ACS Appl. Bio Mater. 3 (2020) 1354–1363, https://doi.org/10.1021/acsabm.9b00956.

[38] M. Mahdavi, A. Fattahi, S. Nouranian, Doxorubicin stability and retention on PEGylated graphene oxide nanocarriers adjacent to human serum albumin, ACS Appl. Bio Mater. 3 (2020) 7646–7653, https://doi.org/10.1021/acsabm.0c00843.

[39] O. Akhavan, E. Ghaderi, H. Emamy, Nontoxic concentrations of PEGylated graphene nanoribbons for selective cancer cell imaging and photothermal therapy, J. Mater. Chem. 22 (2012) 20626–20633, https://doi.org/10.1039/c2jm34330d.

[40] Y. Mo, W. Liu, P. Liu, Q. Liu, Z. Yuan, Q. Wang, D. Yuan, X.-J. Chen, T. Chen, Multifunctional graphene oxide nanodelivery platform for breast cancer treatment, Int. J. Nanomedicine 17 (2022) 6413–6425, https://doi.org/10.2147/IJN.S380447.

[41] H. Wang, J. Zhou, Y. Fu, Y. Zheng, W. Shen, J. Zhou, T. Yin, Deeply infiltrating iRGD-graphene oxide for the intensive treatment of metastatic tumors through PTT-mediated chemosensitization and strengthened integrin targeting-based antimigration, Adv. Healthc. Mater. 10 (2021) e2100536, https://doi.org/10.1002/adhm.202100536.

[42] R.C. Sinclair, P.V. Coveney, Modeling nanostructure in graphene oxide: inhomogeneity and the percolation threshold, J. Chem. Inf. Model. 59 (2019) 2741–2745, https://doi.org/10.1021/acs.jcim.9b00114.

[43] F. Mouhat, F.X. Coudert, M.L. Bocquet, Structure and chemistry of graphene oxide in liquid water from first principles, Nat. Commun. 11 (2020) 1–9, https://doi.org/10.1038/s41467-020-15381-y.

[44] D. Provasi, Ligand-binding calculations with metadynamics, in: Methods in Molecular Biology, Humana Press Inc., 2019, pp. 233–253, https://doi.org/10.1007/978-1-4939-9608-7_10.

[45] S. Raniolo, V. Limongelli, Ligand binding free-energy calculations with funnel metadynamics, Nat. Protoc. 15 (2020) 2837–2866, https://doi.org/10.1038/s41596-020-0342-4.

[46] L. Callea, L. Bonati, S. Motta, Metadynamics-based approaches for modeling the hypoxia-inducible factor 2α ligand binding process, J. Chem. Theory Comput. 17 (2021) 3841–3851, https://doi.org/10.1021/acs.jctc.1c00114.

[47] T. Casalini, K. Treacher, I. Grant, M. Marucci, *In vitro* release from polymeric core/shell nanoparticles through the lens of multiscale modeling, Mol. Pharm. 21 (2024) 2684–2698, https://doi.org/10.1021/acs.molpharmaceut.3c00806.

[48] T. Casalini, Not only in silico drug discovery: molecular modeling towards in silico drug delivery formulations, J. Control. Release 332 (2021) 390–417, https://doi.org/10.1016/j.jconrel.2021.03.005.

[49] S. Motta, P. Siani, E. Donadoni, G. Frigerio, L. Bonati, C. Di Valentin, Metadynamics simulations for the investigation of drug loading on functionalized inorganic nanoparticles, Nanoscale 15 (2023) 7909–7919, https://doi.org/10.1039/D3NR00397C.

[50] Z. Liu, J.T. Robinson, X. Sun, H. Dai, PEGylated nanographene oxide for delivery of water-insoluble cancer drugs, J. Am. Chem. Soc. 130 (2008) 10876–10877, https://doi.org/10.1021/ja803688x.

[51] B. Konkena, S. Vasudevan, Understanding aqueous dispersibility of graphene oxide and reduced graphene oxide through p K_a measurements, J. Phys. Chem. Lett. 3 (2012) 867–872, https://doi.org/10.1021/jz300236w.

[52] O. Akhavan, The effect of heat treatment on formation of graphene thin films from graphene oxide nanosheets, Carbon N. Y. 48 (2010) 509–519, https://doi.org/10.1016/j.carbon.2009.09.069.

[53] H.C. Schniepp, J.-L. Li, M.J. McAllister, H. Sai, M. Herrera-Alonso, D.H. Adamson, R.K. Prud'homme, R. Car, D.A. Saville, I.A. Aksay, Functionalized single graphene sheets derived from splitting graphite oxide, J. Phys. Chem. B 110 (2006) 8535–8539, https://doi.org/10.1021/jp060936f.

[54] M. Xu, J. Zhu, F. Wang, Y. Xiong, Y. Wu, Q. Wang, J. Weng, Z. Zhang, W. Chen, S. Liu, Improved *in vitro* and *in vivo* biocompatibility of graphene oxide through surface modification: poly(acrylic acid)-functionalization is superior to PEGylation, ACS Nano 10 (2016) 3267–3281, https://doi.org/10.1021/acsnano.6b00539.

[55] L. Zhang, Z. Wang, Z. Lu, H. Shen, J. Huang, Q. Zhao, M. Liu, N. He, Z. Zhang, PEGylated reduced graphene oxide as a superior ssRNA delivery system, J. Mater. Chem. B 1 (2013) 749–755, https://doi.org/10.1039/C2TB00096B.

[56] T.-R. Jan, H.-Y. Wu, K.-J. Lin, P.-Y. Wang, Y.-J. Lu, C.-C.M. Ma, H.-W. Yang, C.-W. Lin, Polyethylene glycol-coated graphene oxide attenuates antigen-specific IgE production and enhanced antigen-induced T-cell reactivity in ovalbumin-sensitized BALB/c mice, Int. J. Nanomedicine (2014) 4257, https://doi.org/10.2147/IJN.S66768.

[57] M.A. al-Badri, P. Smith, R.C. Sinclair, K.T. al-Jamal, C.D. Lorenz, Accurate large scale modelling of graphene oxide: ion trapping and chaotropic potential at the interface, Carbon N. Y. 174 (2021) 266–275, https://doi.org/10.1016/j.carbon.2020.12.032.

[58] E. Peng, N. Todorova, I. Yarovsky, Effects of size and functionalization on the structure and properties of graphene oxide nanoflakes: an in silico investigation, ACS Omega 3 (2018) 11497–11503, https://doi.org/10.1021/acsomega.8b00866.

[59] C.D. Williams, M. Lísal, Coarse grained models of graphene and graphene oxide for use in aqueous solution, 2d Mater 7 (2020) 025025, https://doi.org/10.1088/2053-1583/ab6f0c.

[60] E. Donadoni, P. Siani, G. Frigerio, C. Milani, Q. Cui, C. Di Valentin, The effect of polymer coating on nanoparticles' interaction with lipid membranes studied by coarse-grained molecular dynamics simulations, Nanoscale 16 (2024) 9108–9122, https://doi.org/10.1039/D4NR00495G.

[61] R. García-Álvarez, M. Vallet-Regí, Hard and soft protein corona of nanomaterials: analysis and relevance, Nanomaterials 11 (2021) 888, https://doi.org/10.3390/nano11040888.

[62] G. Speelmans, R.W. Staffhorst, B. de Kruijff, F.A. de Wolf, Transport studies of doxorubicin in model membranes indicate a difference in passive diffusion across and binding at the outer and inner leaflets of the plasma membrane, Biochemistry 33 (1994) 13761–13768, https://doi.org/10.1021/bi00250a029.

[63] V. Subasinghege Don, L. Kim, R. David, J.A. Nauman, R. Kumar, Adsorption studies at the graphene oxide–liquid interface: a molecular dynamics study, J. Phys. Chem. C 127 (2023) 5920–5930, https://doi.org/10.1021/acs.jpcc.2c07080.

[64] E. Song, W. Han, C. Li, D. Cheng, L. Li, L. Liu, G. Zhu, Y. Song, W. Tan, Hyaluronic acid-decorated graphene oxide nanohybrids as nanocarriers for targeted and pH-responsive anticancer drug delivery, ACS Appl. Mater. Interfaces 6 (2014) 11882–11890, https://doi.org/10.1021/am502423r.

[65] L. Feng, Z. Dong, D. Tao, Y. Zhang, Z. Liu, The acidic tumor microenvironment: a target for smart cancer nano-theranostics, Natl. Sci. Rev. 5 (2018) 269–286, https://doi.org/10.1093/NSR/NWX062.

[66] M.J. Geisow, W.H. Evans, pH in the endosome: measurements during pinocytosis and receptor-mediated endocytosis, Exp. Cell Res. 150 (1984) 36–46, https://doi.org/10.1016/0014-4827(84)90699-2.

[67] Y. Lv, L. Tao, S.W. Annie Bligh, H. Yang, Q. Pan, L. Zhu, Targeted delivery and controlled release of doxorubicin into cancer cells using a multifunctional graphene oxide, Mater. Sci. Eng. C 59 (2016) 652–660, https://doi.org/10.1016/j.msec.2015.10.065.

[68] M. Hashemi, A. Yadegari, G. Yazdanpanah, M. Omidi, S. Jabbehdari, F. Haghiralsadat, F. Yazdian, L. Tayebi, Normalization of doxorubicin release from graphene oxide: new approach for optimization of effective parameters on drug loading, Biotechnol. Appl. Biochem. 64 (2017) 433–442, https://doi.org/10.1002/BAB.1487.

[69] D. Depan, J. Shah, R.D.K. Misra, Controlled release of drug from folate-decorated and graphene mediated drug delivery system: synthesis, loading efficiency, and drug release response, Mater. Sci. Eng. C 31 (2011) 1305–1312, https://doi.org/10.1016/J.MSEC.2011.04.010.

[70] M. Rezaian, R. Maleki, M.D. Dahroud, A. Alamdari, M. Alimohammadi, pH-sensitive co-adsorption/release of doxorubicin and paclitaxel by carbon nanotube, fullerene, and graphene oxide in combination with N-isopropylacrylamide: a molecular dynamics study, Biomolecules 8 (2018) 127, https://doi.org/10.3390/BIOM8040127.

[71] H. Hashemzadeh, H. Raissi, Understanding loading, diffusion and releasing of doxorubicin and paclitaxel dual delivery in graphene and graphene oxide carriers as highly efficient drug delivery systems, Appl. Surf. Sci. 500 (2020) 144220, https://doi.org/10.1016/J.APSUSC.2019.144220.

[72] A. Zaboli, H. Raissi, H. Hashemzadeh, F. Farzad, Graphene oxide hosting a pH-sensitive prodrug: an in silico investigation of graphene oxide-based nanovehicle toward cancer therapy, ACS Appl. Bio Mater. 6 (2023) 2826–2836, https://doi.org/10.1021/acsabm.3c00276.

[73] Q.H. Le, F. Neila, K. Smida, Z. Li, Z. Abdelmalek, I. Tlili, pH-responsive anticancer drug delivery systems: insights into the enhanced adsorption and release of DOX drugs using graphene oxide as a nanocarrier, Eng. Anal. Bound. Elem. 157 (2023) 157–165, https://doi.org/10.1016/J.ENGANABOUND.2023.09.008.

[74] A. Bina, H. Raissi, H. Hashemzadeh, F. Farzad, Conjugation of a smart polymer to doxorubicin through a pH-responsive bond for targeted drug delivery and improving drug loading on graphene oxide, RSC Adv. 11 (2021) 18809–18817, https://doi.org/10.1039/D1RA02361F.

[75] F.A. Carey, R.J. Sundberg, Advanced Organic Chemistry, Springer US, Boston, MA, 2007, https://doi.org/10.1007/978-0-387-44899-2.

[76] Y. Pocker, B.P. Ronald, K.W. Anderson, Epoxides in vicinal diol dehydration. 7. A mechanistic characterization of the spontaneous ring opening process of epoxides in aqueous solution: kinetic and product studies, J. Am. Chem. Soc. 110 (1988) 6492–6497, https://doi.org/10.1021/ja00227a033.

[77] R. David, R. Kumar, Reactive events at the graphene oxide–water interface, Chem. Commun. 57 (2021) 11697–11700, https://doi.org/10.1039/D1CC04589J.

[78] A. Lerf, H. He, M. Forster, J. Klinowski, Structure of graphite oxide revisited, J. Phys. Chem. B 102 (1998) 4477–4482, https://doi.org/10.1021/jp9731821.

[79] Y.Y. Khine, X. Ren, D. Chu, Y. Nishina, T. Foller, R. Joshi, Surface functionalities of graphene oxide with varying flake size, Ind. Eng. Chem. Res. 61 (2022) 6531–6536, https://doi.org/10.1021/acs.iecr.2c00748.

[80] B. Alberto Arenas-Blanco, L. Muñoz-Rugeles, R. Cabanzo-Hernández, E. Mejía-Ospino, Molecular dynamics study of the effect on the interfacial activity of alkylamine-modified graphene oxide, J. Mol. Liq. 362 (2022) 119724, https://doi.org/10.1016/j.molliq.2022.119724.

[81] E. Jurrus, D. Engel, K. Star, K. Monson, J. Brandi, L.E. Felberg, D.H. Brookes, L. Wilson, J. Chen, K. Liles, M. Chun, P. Li, D.W. Gohara, T. Dolinsky, R. Konecny, D.R. Koes, J.E. Nielsen, T. Head-Gordon, W. Geng, R. Krasny, G. Wei, M.J. Holst, J.A. McCammon, N.A. Baker, Improvements to the APBS biomolecular solvation software suite, Protein Sci. 27 (2018) 112–128, https://doi.org/10.1002/pro.3280.

[82] W. Humphrey, A. Dalke, K. Schulten, VMD: visual molecular dynamics, J. Mol. Graph. 14 (1996) 33–38, https://doi.org/10.1016/0263-7855(96)00018-5.

[83] W.L. Jorgensen, D.S. Maxwell, J. Tirado-Rives, Development and testing of the OPLS all-atom force field on conformational energetics and properties of organic liquids, J. Am. Chem. Soc. 118 (1996) 11225–11236, https://doi.org/10.1021/ja9621760.

[84] W.L. Jorgensen, J. Chandrasekhar, J.D. Madura, R.W. Impey, M.L. Klein, Comparison of simple potential functions for simulating liquid water, J. Chem. Phys. 79 (1983) 926–935, https://doi.org/10.1063/1.445869.

[85] N.A. Garcia, J.B. Awuah, C. Zhao, F. Vuković, T.R. Walsh, Simulation-ready graphene oxide structures with hierarchical complexity: a modular tiling strategy, 2d Mater 10 (2023) 025007, https://doi.org/10.1088/2053-1583/acb0e1.

[86] B. Zheng, Y. Tian, S. Jia, X. Zhao, H. Li, Molecular dynamics study on applying layered graphene oxide membranes for separating cadmium ions from water, J. Membr. Sci. 603 (2020) 117996, https://doi.org/10.1016/J.MEMSCI.2020.117996.

[87] Y. Wu, C.-F. Fu, Q. Huang, P. Zhang, P. Cui, J. Ran, J. Yang, T. Xu, 2D heterostructured nanofluidic channels for enhanced desalination performance of graphene oxide membranes, ACS Nano 15 (2021) 7586–7595, https://doi.org/10.1021/acsnano.1c01105.

[88] D. Bahamon, L.F. Vega, Molecular simulations of phenol and ibuprofen removal from water using multilayered graphene oxide membranes, Mol. Phys. 117 (2019) 3703–3714, https://doi.org/10.1080/00268976.2019.1662129.

[89] L.S. Dodda, J.Z. Vilseck, J. Tirado-Rives, W.L. Jorgensen, 1.14*CM1A-LBCC: localized bond-charge corrected CM1A charges for condensed-phase simulations, J. Phys. Chem. B 121 (2017) 3864–3870, https://doi.org/10.1021/acs.jpcb.7b00272.

[90] L.S. Dodda, I. Cabeza de Vaca, J. Tirado-Rives, W.L. Jorgensen, LigParGen web server: an automatic OPLS-AA parameter generator for organic ligands, Nucleic Acids Res. 45 (2017) W331–W336, https://doi.org/10.1093/nar/gkx312.

[91] W.L. Jorgensen, J. Tirado-Rives, Potential energy functions for atomic-level simulations of water and organic and biomolecular systems, Proc. Natl. Acad. Sci. 102 (2005) 6665–6670, https://doi.org/10.1073/pnas.0408037102.

[92] M.J. Abraham, T. Murtola, R. Schulz, S. Páll, J.C. Smith, B. Hess, E. Lindahl, GROMACS: high performance molecular simulations through multi-level parallelism from laptops to supercomputers, SoftwareX 1–2 (2015) 19–25, https://doi.org/10.1016/j.softx.2015.06.001.

[93] G. Bussi, D. Donadio, M. Parrinello, Canonical sampling through velocity rescaling, J. Chem. Phys. 126 (2007) 014101, https://doi.org/10.1063/1.2408420.

[94] M. Parrinello, A. Rahman, Polymorphic transitions in single crystals: a new molecular dynamics method, J. Appl. Phys. 52 (1981) 7182–7190, https://doi.org/10.1063/1.328693.
[95] T. Darden, D. York, L. Pedersen, Particle mesh Ewald: An N·log(N) method for Ewald sums in large systems, J. Chem. Phys. 98 (1993) 10089–10092, https://doi.org/10.1063/1.464397.
[96] A. Bondi, van der Waals Volumes and Radii, J. Phys. Chem. 68 (1964) 441–451, https://doi.org/10.1021/j100785a001.
[97] S. Motta, P. Siani, A. Levy, C. Di Valentin, Exploring the drug loading mechanism of photoactive inorganic nanocarriers through molecular dynamics simulations, Nanoscale 13 (2021) 13000–13013, https://doi.org/10.1039/D1NR01972D.
[98] M. Bonomi, G. Bussi, C. Camilloni, G.A. Tribello, P. Banáš, A. Barducci, M. Bernetti, P.G. Bolhuis, S. Bottaro, D. Branduardi, R. Capelli, P. Carloni, M. Ceriotti, A. Cesari, H. Chen, W. Chen, F. Colizzi, S. De, M. De La Pierre, D. Donadio, V. Drobot, B. Ensing, A.L. Ferguson, M. Filizola, J.S. Fraser, H. Fu, P. Gasparotto, F.L. Gervasio, F. Giberti, A. Gil-Ley, T. Giorgino, G.T. Heller, G. M. Hocky, M. Iannuzzi, M. Invernizzi, K.E. Jelfs, A. Jussupow, E. Kirilin, A. Laio, V. Limongelli, K. Lindorff-Larsen, T. Löhr, F. Marinelli, L. Martin-Samos, M. Masetti, R. Meyer, A. Michaelides, C. Molteni, T. Morishita, M. Nava, C. Paissoni, E. Papaleo, M. Parrinello, J. Pfaendtner, P. Piaggi, G.M. Piccini, A. Pietropaolo, F. Pietrucci, S. Pipolo, D. Provasi, D. Quigley, P. Raiteri, S. Raniolo, J. Rydzewski, M. Salvalaglio, G.C. Sosso, V. Spiwok, J. Šponer, D.W. H. Swenson, P. Tiwary, O. Valsson, M. Vendruscolo, G.A. Voth, A. White, Promoting transparency and reproducibility in enhanced molecular simulations, Nat. Methods 16 (2019) 670–673, https://doi.org/10.1038/s41592-019-0506-8.
[99] G.A. Tribello, M. Bonomi, D. Branduardi, C. Camilloni, G. Bussi, PLUMED 2: new feathers for an old bird, Comput. Phys. Commun. 185 (2014) 604–613, https://doi.org/10.1016/j.cpc.2013.09.018.
[100] D. Branduardi, G. Bussi, M. Parrinello, Metadynamics with adaptive Gaussians, J. Chem. Theory Comput. 8 (2012) 2247–2254, https://doi.org/10.1021/ct3002464.
[101] S. Motta, L. Callea, L. Bonati, A. Pandini, PathDetect-SOM: a neural network approach for the identification of pathways in ligand binding simulations, J. Chem. Theory Comput. 18 (2022) 1957–1968, https://doi.org/10.1021/acs.jctc.1c01163.
[102] R. Wehrens, L.M.C. Buydens, Self- and super-organizing maps in R: the kohonen package, J. Stat. Softw. 21 (2007) 1–19, https://doi.org/10.18637/JSS.V021.I05.
[103] R. Wehrens, J. Kruisselbrink, Flexible self-organizing maps in kohonen 3.0, J. Stat. Softw. 87 (2018) 1–18, https://doi.org/10.18637/JSS.V087.I07.
[104] G. Frigerio, E. Donadoni, P. Siani, J. Vertemara, S. Motta, L. Bonati, L. De Gioia, C. Di Valentin, Mechanism of RGD-conjugated nanodevice binding to its target protein integrin $\alpha_v\beta_3$ by atomistic molecular dynamics and machine learning, Nanoscale 16 (2024) 4063–4081, https://doi.org/10.1039/D3NR05123D.
[105] E. Donadoni, G. Frigerio, P. Siani, S. Motta, J. Vertemara, L. De Gioia, L. Bonati, C. Di Valentin, Molecular dynamics for the optimal design of functionalized nanodevices to target folate receptors on tumor cells, ACS Biomater. Sci. Eng. 9 (2023) 6123–6137, https://doi.org/10.1021/acsbiomaterials.3c00942.
[106] T. Kohonen, Essentials of the self-organizing map, Neural Netw. 37 (2013) 52–65, https://doi.org/10.1016/j.neunet.2012.09.018.